

# Multiple Stellar Populations of Globular Clusters From Homogeneous Ca–CN–CH–NH Photometry. VII. Metal-Poor Populations in 47 Tucanae (NGC 104) <sup>\*†</sup>

JAE-WOO LEE<sup>1</sup>

<sup>1</sup>*Department of Physics and Astronomy, Sejong University  
209 Neungdong-ro, Gwangjin-Gu, Seoul, 05006, Republic of Korea  
jaewoolee@sejong.ac.kr, jaewoolee@sejong.edu*

## ABSTRACT

We present new large field-of-view ( $\sim 1^\circ \times 1^\circ$ ) Ca–CN photometry of the prototypical metal-rich globular cluster 47 Tucanae (NGC 104). Our results are the following. (1) The populational number ratios of the red giant branch (RGB) and red horizontal branch (RHB) are in excellent agreement:  $n(\text{CN-w}):n(\text{CN-s}) = 30:70$  ( $\pm 1-2$ ), where the CN-w and CN-s stand for the CN-weak and CN-strong populations, respectively. Both the CN-s RGB and RHB populations are more centrally concentrated than those of CN-w populations are. (2) Our photometric metallicities of individual RGB stars in each population can be well described by bimodal distributions with two metallicity peaks,  $[\text{Fe}/\text{H}] \sim -0.72$  and  $-0.92$  dex, where the metal-poor components occupy  $\sim 13\%$  of the total RGB stars. The metal-poor populations are more significantly centrally concentrated than the metal-rich populations, showing a similar result that we found in M3. (3) The RGB bump  $V$  magnitudes of individual populations indicate that there is no difference in the helium abundance between the two metal-poor populations, while the helium enhancement of  $\Delta Y \sim 0.02-0.03$  is required between the two metal-rich populations. (4) The RHB morphology of 47 Tuc appears to support our idea of the bimodal metallicity distribution of the cluster. We suggest that 47 Tuc could be another example of merger remnants of two globular clusters, similar to M3 and M22.

**Keywords:** Stellar populations (1622); Population II stars (1284); Hertzsprung Russell diagram (725); Globular star clusters (656); Chemical abundances (224); Stellar evolution (1599); Red giant branch (1368); Red giant bump (1369); Horizontal branch stars (746)

## 1. INTRODUCTION

The ubiquitous nature of the multiple populations (MPs) in globular clusters (GCs) is an enigmatic phenomenon that cannot be easily understood in modern astrophysics (e.g., see Bastian & Lardo 2018; Gratton et al. 2019; Cassisi & Salaris 2021). Once thought to be simple groups of old stars, not only the Galactic but also the extra-Galactic GCs show MPs containing at least two populations: One is called first generation (FG) with chemical compositions similar to abundance patterns observed in Galactic field stars with the same metallicity, while the other is called a second generation (SG) showing the chemical compositions that experienced proton capture processes at high temperature. Most notably, the so-called Na–O and C–N anticorrelations are thought to be a

strong evidence of the MPs in GCs (Carretta et al. 2009; Lee 2010).

Recent development of numerical simulations may seem promising to delineate the formation of GCs with MPs (e.g., D’ercole et al. 2008; Bekki 2019; Calura et al. 2019; McKenzie & Bekki 2021; Lacchin et al. 2021), however, some fundamental processes that induce the chemical evolution between MPs are yet to be understood (e.g., see Bastian et al. 2015; Renzini et al. 2015; Bastian & Lardo 2018; Gratton et al. 2019).

47 Tuc (NGC 104) is a massive nearby GC, that has long been considered as a prototypical metal-rich GC (e.g., Hesser et al. 1987). Numerous photometric and spectroscopic studies have been conducted for this cluster. Elemental abundance variations in the red giant branch (RGB), red horizontal branch (RHB), and main-sequence (MS) stars in 47 Tuc had been known for decades long before the establishment of the MPs in GCs during the last decade.

Hesser (1978) employed low-resolution spectroscopy, and he found that there exist CN abundance variations from RGB to MS stars in 47 Tuc (see also Briley et al. 1991, 2004; Cannon et al. 1998; Harbeck 2003, for the abundance variation in MS stars in 47 Tuc). Norris & Freeman (1979) confirmed this result, and they concluded that the primordial elemental abundance difference is responsible for such CN

<sup>\*</sup> Based on observations made with the Cerro Tololo Inter-American Observatory (CTIO) 1 m telescope, which is operated by the SMARTS consortium.

<sup>†</sup> This work presents results from the European Space Agency (ESA) space mission Gaia. Gaia data are being processed by the Gaia Data Processing and Analysis Consortium (DPAC). Funding for the DPAC is provided by national institutions, in particular the institutions participating in the Gaia MultiLateral Agreement (MLA). The Gaia mission website is <https://www.cosmos.esa.int/gaia>. The Gaia archive website is <https://archives.esac.esa.int/gaia>.

anomalies (see also [Cottrell & Da Costa 1981](#), who drew the same conclusion from the Na–CN positive correlation). The primordial origin of MPs in 47 Tuc was securely confirmed by [Carretta et al. \(2004\)](#), who revealed the Na–O anticorrelation in the turn-off and the base of RGB stars in 47 Tuc. Later, [Milone et al. \(2012\)](#) nicely demonstrated that the MS split in 47 Tuc can be ascribed to the different helium and light elemental abundances, such as CNO, that can be seen in GC MPs. They also found a radial gradient in the CN abundance, in the sense that the CN-s RGB stars are more centrally concentrated than the CN-w RGB stars are, where the CN weak and strong stars are defined to be stars with weak and strong CN absorption bands at  $\lambda 3883$  at a given  $V$  magnitude (see also [Chun & Freeman 1979](#); [Smith 1979](#); [Briley 1997](#); [Nataf et al. 2011](#)).

Not only the RGB stars but also the RHB stars in 47 Tuc also display the prototypical characteristics of MPs. [Norris & Freeman \(1982\)](#) found that there exist a CN–CH anticorrelation in the RHB stars in 47 Tuc, and  $V$  magnitude of the CN-s RHB stars is  $\Delta V \sim 0.04$  mag brighter than the CN-w counterparts, which led them to conclude that differences in helium abundance or helium core mass are responsible for this luminosity difference between the two groups. [Briley \(1997\)](#) confirmed this result, and they also noted that the CN-s RHB stars tend to be bluer than the CN-w RHB stars (see also [Nataf et al. 2011](#)). In a similarly context, [Gratton et al. \(2013\)](#) found that sodium abundances increase toward bluer color along the RHB in 47 Tuc, which can be understood from the existence of the Na–CN positive correlation as we mentioned above.

The presence of the subgiant branch (SGB) split in 47 Tuc also indicates that it is not composed of a simple stellar population. After the monumental discovery of the double SGB sequence in NGC 1851 ([Milone et al. 2008](#); [Cassisi et al. 2008](#)), [Anderson et al. \(2009\)](#) reanalyzed a large number of Hubble Space Telescope (HST) archival data, and they found the existence of the double SGB in 47 Tuc, where the second SGB sequence is  $\sim 0.05$  mag fainter than the main SGB body and occupies  $\sim 10\%$  of the stars. They also noted that there exists intrinsic color dispersion in the MS stars, which can be ascribed to the metallicity spread (with standard helium abundance) or a helium abundance dispersion of  $\Delta Y = 0.026$  (see also [Milone et al. 2012](#)). [Di Criscienzo et al. \(2010\)](#) interpreted that, in addition to the helium abundance variations in the 47 Tuc, the difference in the C+N+O abundance could be responsible for the double SGB in 47 Tuc, in the sense that the fainter SGB stars contain higher overall C+N+O abundance than the brighter ones. Later, [Marino et al. \(2016\)](#) performed a spectroscopic study for SGB stars, finding no concrete evidence of a C+N+O enhancement in the faint SGB stars.

Finally, the RGB bump (RGBB) of 47 Tuc also indicates that it is a very intriguing cluster. [Nataf et al. \(2011\)](#) found that RGBB  $V$  magnitude becomes fainter with the radial distance from the cluster’s center.

In our previous study, we showed that M3, previously considered as a monometallic prototypical GC, has two groups

of stars with different metallicity,  $\Delta[\text{Fe}/\text{H}] \sim 0.15$  dex. More recently, independent studies showed some evidence of a metallicity spread in the FG in previously considered monometallic GCs and different metallicity distributions between the FG and SG (e.g., [Legnardi et al. 2022](#); [Lardo et al. 2022](#)), making the understanding of the formation of GCs a more formidable task.

In this paper, we investigate 47 Tuc using our own photometric system that is optimized to study the GC MPs. So far, almost all the previous studies of the cluster assumed that 47 Tuc shows an unimodal metallicity distribution (see also [Gratton et al. 2019](#)). Interestingly, our results will show that 47 Tuc shows a bimodal metallicity distribution with a metallicity difference of  $\Delta[\text{Fe}/\text{H}] \sim 0.2$  dex, which can be also supported by the RGBB magnitude and the RHB morphology. Our finding will set a crucial constraint to understand the formation of 47 Tuc.

## 2. SPECTROSCOPIC METALLICITY DISTRIBUTIONS OF 47 TUC

Thanks to the advance in high throughput (multiobject) spectrographs combined with large aperture telescopes, utility of high-resolution spectroscopy becomes more important. However, there appears to exist some limitations that significantly reduce the capability of spectroscopic study of GCs. For example, RGB stars in metal-rich GC 47 Tuc show very strong absorption lines combined with severe degree of line blendings that make accurate elemental abundance measurements somewhat difficult (see also [Lee 2010, 2016](#)). Not surprisingly, unequivocal results among different research groups can often be witnessed.

In Figure 1(a), we show a comparison of the  $[\text{Fe}/\text{H}]$  measurements for 28 RGB stars in 47 Tuc in common with [Carretta et al. \(2009\)](#) and [Codero et al. \(2014\)](#). Using these 28 stars, we obtained the similar mean  $[\text{Fe}/\text{H}]$  values between the two studies:  $\langle[\text{Fe}/\text{H}]\rangle = -0.739 \pm 0.028 \pm 0.005$  dex from [Carretta et al. \(2009\)](#) and  $-0.769 \pm 0.075 \pm 0.014$  dex from [Codero et al. \(2014\)](#). However, the  $[\text{Fe}/\text{H}]$  distributions of individual stars may tell a completely different story as shown in the figure. The  $[\text{Fe}/\text{H}]$  distribution of [Carretta et al. \(2009\)](#) appears to be an unimodal, while that of [Codero et al. \(2014\)](#) is a nonunimodal with a significantly large dispersion. We performed statistical tests to see if these two  $[\text{Fe}/\text{H}]$  distributions are unimodal. The  $p$ -value returned from our dip test is  $1.85 \times 10^{-3}$  for [Codero et al. \(2014\)](#), indicating that it is nonunimodal. On the other hand, the  $p$ -value of that of [Carretta et al. \(2009\)](#) is 0.922, and it is most likely a unimodal, as our histogram suggested. In the figure, the red-filled circles show the RGB stars measured by using the same instrument (FLAMES-GIRAFFE on the Very Large Telescope Kueyen telescope) between the two studies, exhibiting large differences. Therefore, the discrepancy between the two studies is not instrument dependent, but it may have something to do with data analysis procedures in each research group.

In Figure 1(d), we show histograms for  $[\text{Fe}/\text{H}]$  distributions of individual stars in 47 Tuc from various studies

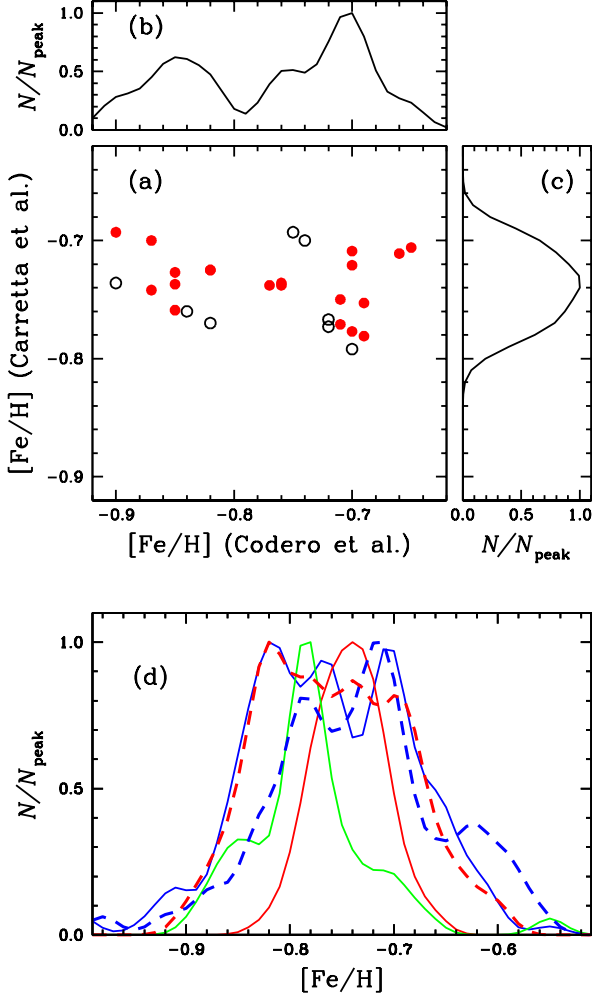


**Figure 1.** (a) Comparison of  $[\text{Fe}/\text{H}]$  of Carretta et al. (2009) against that of Codero et al. (2014) for 28 RGB stars in 47 Tuc in common between the two studies. The filled red circles indicate the RGB stars using the same instrument between the two studies. (b) Histogram of the  $[\text{Fe}/\text{H}]$  distribution by Codero et al. (2014). (c) Histogram of the  $[\text{Fe}/\text{H}]$  distribution by Carretta et al. (2009). (d) Histograms of the  $[\text{Fe}/\text{H}]$  measurements from literature. The red, blue, and green solid lines are for the RGB stars by Carretta et al. (2009), Codero et al. (2014), and Wang et al. (2017). The thick red dashed line is for the RHB stars by Gratton et al. (2013), while the thick blue dashed line is for the SGB stars by Marino et al. (2016). Except for the RGB  $[\text{Fe}/\text{H}]$  distribution by Carretta et al. (2009), other four measurements show nonunimodal  $[\text{Fe}/\text{H}]$  distributions with large metallicity dispersions.

(Carretta et al. 2009; Codero et al. 2014; Gratton et al. 2013; Marino et al. 2016; Wang et al. 2017). The figure clearly shows that the  $[\text{Fe}/\text{H}]$  distribution of 47 Tuc is not likely unimodal with large metallicity dispersions, except for that of Carretta et al. (2009).

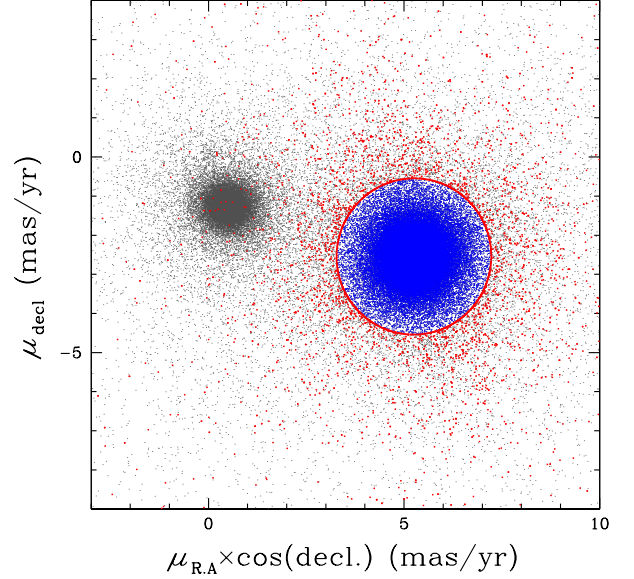


**Figure 2.** Gaia EDR3 proper-motions of our FOV. The red ellipse indicates the boundary ( $3\sigma$ ) of the 47 Tuc member stars shown with blue dots. The red dots are stars located within 300'' from 47 Tuc, and they are classified as nonmember stars based on the proper-motion study.

We are left with the impression that  $\Delta[\text{Fe}/\text{H}] \sim 0.1 - 0.2$  dex from high-resolution spectroscopy can be introduced, which may hamper revealing small-scale structures in the metallicity distribution of given stellar populations (see also Lee 2010, 2016; Lee & Sneden 2021). In this regard, our narrow- and intermediate-band photometry can be a valuable asset to investigate metallicity distributions, for example, of the MPs in GCs.

### 3. OBSERVATIONS AND DATA REDUCTION

Observations for 47 Tuc were carried out in 54 nights, 27 of which were photometric, in 9 runs from September 2007 to August 2013 using the CTIO 1.0m telescope. The CTIO 1.0m telescope was equipped with a STA  $4k \times 4k$  CCD camera, providing a plate scale of  $0''.289 \text{ pixel}^{-1}$  and a field-of-view (FOV) of about  $20' \times 20'$ . The detailed discussion of our new filter system can be found in Lee (2017). During the whole seasons, the average seeing of our 47 Tuc science frames was  $1''.37 \pm 0''.20$ . The effective FOV of our 47 Tuc science field was about  $1^\circ \times 1^\circ$  except for the JWL39 filter. We employed our JWL39 filter only in 2013, and it mostly covered an FOV of  $20' \times 20'$  of the central part of the cluster.

The detailed procedures for the raw data handling were described in our previous works (Lee et al. 2014; Lee 2015, 2017; Lee & Pogge 2016). The photometry of the cluster and photometric standard frames were analyzed using DAOPHOTII, DAOGROW, ALLSTAR and ALLFRAME, and associate packages (Stetson 1987, 1994; Lee & Carney

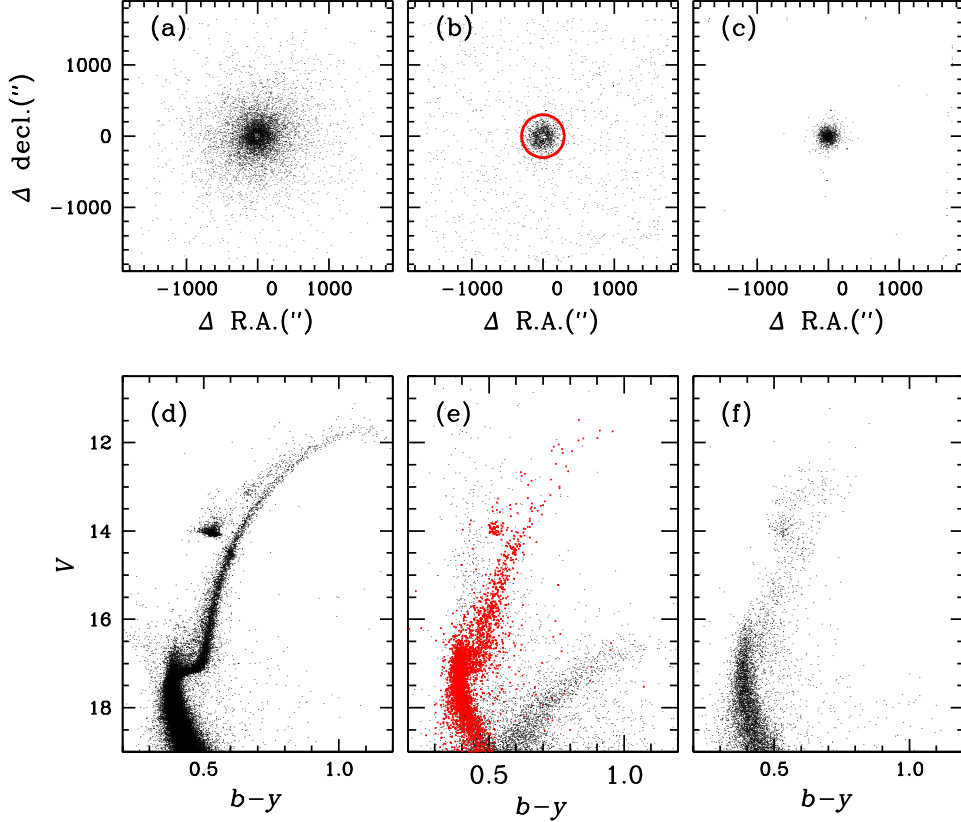


**Figure 3.** (a) Positions of bright stars with  $V \leq 17$  mag that match with the Gaia EDR3 and classified as 47 Tuc’s members. (b) Positions of bright stars with  $V \leq 17$  mag that match with the Gaia EDR3 but classified as 47 Tuc’s nonmembers. The thick red circle indicates the radial distance of  $300''$  from the cluster’s center. (c) Positions of bright stars with  $V \leq 17$  mag that have no counterpart in the Gaia EDR3. (d)  $(b-y)$  versus  $V$  CMD for (a). (e)  $(b-y)$  versus  $V$  CMD for (b). Note the presence of the SMC stars in the faint regime. The red dots show the CMD from stars located within  $300''$  from the center that are considered as proper-motion nonmembers of the cluster. (f)  $(b-y)$  versus  $V$  CMD for stars with no Gaia EDR3 counterpart.

1999). The total number of stars measured from our ALL-FRAME run was about 111,000.

Astrometric solutions for individual stars in our field were derived using the data extracted from the Gaia EDR3 (Gaia Collaboration 2021) and the IRAF IMCOORS package. Then the astrometric solution was applied to calculate the equatorial coordinates for all stars measured in our science frames.

#### 4. MEMBERSHIP SELECTION

The Galactic latitude of 47 Tuc is large,  $b = -45^\circ$ , and the contamination from the foreground off-cluster Galactic field stars is expected to be small. On the other hand, due to the proximity to the Small Magellanic Cloud (SMC), the contamination from the SMC can be severe, in particular for the faint regime. In Figure 2, we show the proper-motions for our 47 Tuc’s FOV from the Gaia EDR3 (Gaia Collaboration 2021), where two groups of stars, one for 47 Tuc and the other for the SMC, can be clearly seen.

In order to select proper-motion member stars, we derived the mean values of proper-motions of 47 Tuc using iterative

$\sigma$ -clipping calculations, finding that, in units of milliarcsecond per year,  $(\mu_{\text{RA}} \times \cos \delta, \mu_{\text{decl}}) = (5.253, -2.543)$  with standard deviations along the major axis of the ellipse of  $0.666 \text{ mas yr}^{-1}$  and along the minor axis of  $0.659 \text{ mas yr}^{-1}$ . We considered that stars within  $3\sigma$  from the mean values are 47 Tuc proper-motion member stars as shown with blue dots in Figure 2.

In Figure 3, we show color-magnitude diagrams (CMDs) for proper-motion members and nonmembers of 47 Tuc. Also shown are the stars without the Gaia EDR3 counterparts. We believe that, due to large measurement uncertainties rising from crowdedness, a significant fraction of 47 Tuc member stars in the central part deviates large in the proper-motion measurements of the Gaia EDR3 as shown in Figure 2. Furthermore, there exists a large number of stars located in the central part of cluster, owing to crowdedness, without proper-motion measurements. In our current paper, we consider RGB stars with  $-1.5 \leq V - V_{\text{HB}} \leq 2.5$  mag in two cases separately: (1) using proper-motion member stars only (case (1)), where our sample is not complete and tends to be slightly biased toward the outer part of the cluster; (2) using



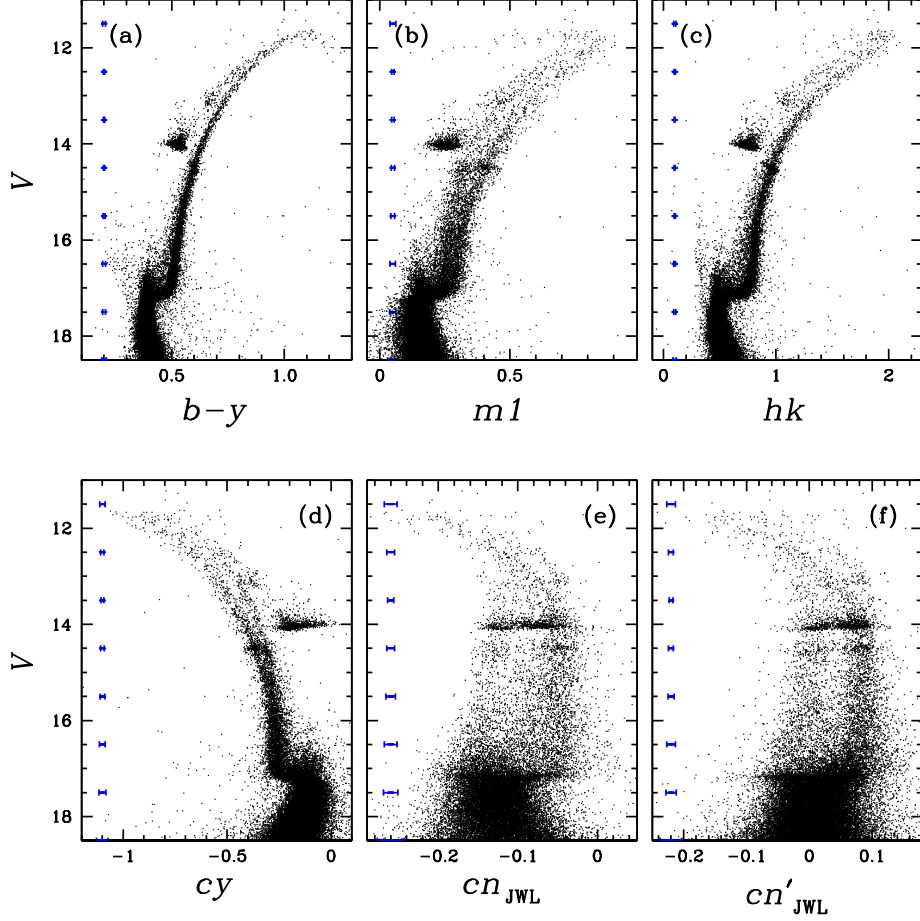


**Figure 4.** CMDs for proper-motion membership stars in 47 Tuc. We also show the mean measurement uncertainties at a given  $V$  magnitude bin with blue error bars. Note the broad RGB sequences in  $m1$ ,  $cy$  and the discrete double RGB sequences in  $cn_{JWL}$  and  $cn'_{JWL}$  CMDs.

stars selected from the multicolor CMDs (case (2)), which include the stars in case (1) and missing member stars by Gaia EDR3 as shown in Figure 2.

## 5. PHOTOMETRIC INDICES AND COLOR-MAGNITUDE DIAGRAMS

We used the filters provided by the CTIO from 2007 to 2010, and we used our own filters since 2012. As we already noted in our previous study (Lee 2015, 2019c), the original  $Ca_{CTIO}$  was designed to have a filter bandwidth and pivot wavelength very similar to that of the  $Ca_{AT}$  defined by Anthony-Twarog et al. (1991). Due to aging, the  $Ca_{CTIO}$  had been significantly altered to the shorter wavelength, resulting in having the passband similar to our JWL39 filter (e.g., see Figure 1 of Lee 2019c). Therefore, we do not use the  $Ca_{CTIO}$  to measure metallicity. Instead, we used the  $Ca_{CTIO}$  as a good proxy of the JWL39 filter in our current study.

Throughout this work, we will use our own photometric indices (see also Lee 2019c; Lee & Sneden 2021), defined

as

$$hk_{JWL} = (Ca_{JWL} - b) - (b - y). \quad (1)$$

$$cn_{JWL} = JWL39 - Ca_{JWL}, \quad (2)$$

$$cn'_{JWL} = Ca_{CTIO} - Ca_{JWL}. \quad (3)$$

The  $hk_{JWL}$  index is a good photometric measure of metallicity (e.g., Anthony-Twarog et al. 1991; Lee et al. 2009; Lee 2015), assuming a constant  $[Ca/Fe]$  among GC membership stars (Carney 1996; Marino et al. 2019). As we already discussed (Lee 2019c), the  $cn'_{JWL}$  can be used as an excellent proxy of the  $cn_{JWL}$  index. Hence, both the  $cn_{JWL}$  and  $cn'_{JWL}$  indices are photometric measures of the CN band at  $\lambda 3883$ .

In Figure 4, we show our CMDs. The discrete RGB sequences can be clearly seen both in our  $cn_{JWL}$  and  $cn'_{JWL}$  CMDs. On the other hand, both the  $m1$  and  $cy$  CMDs show splits in the upper RGB sequences but not in the lower RGB sequences.

## 6. RED GIANT BRANCH

### 6.1. Populational Tagging

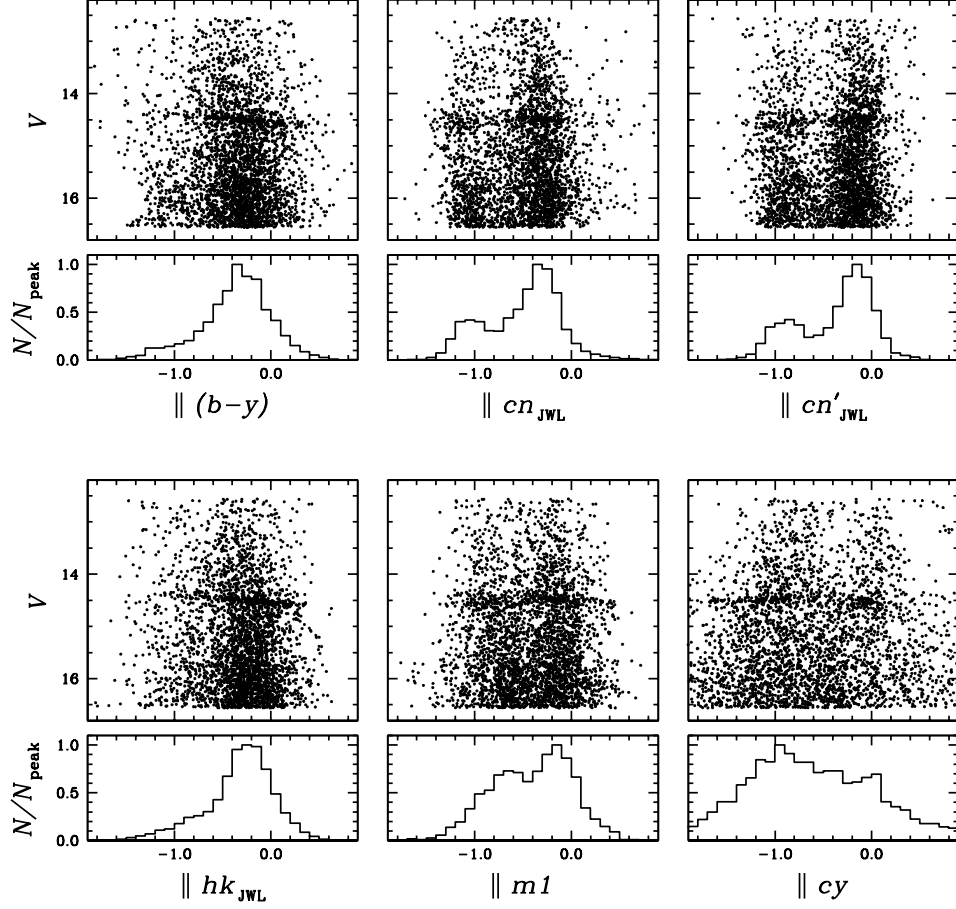


**Figure 5.** Parallelized CMDs with histograms for various color indices used in our study. Note that our  $\|cn_{JWL}$  and  $\|cn'_{JWL}$  indices show discrete double RGB sequences in 47 Tuc. We also note that both the  $\|(b-y)$  and  $\|hk_{JWL}$ , both of which are good metallicity indicators, show asymmetric distributions toward smaller color indices.

We followed the similar method that we developed in our previous studies of other GCs with MPs (e.g., see Lee & Sneden 2021; Lee 2021). In order to remove the luminosity effect in our analysis, the RGB sequences in the individual color indices were parallelized using the following relation (also see Lee 2019a,c);

$$\|CI(x) \equiv \frac{CI(x) - CI_{red}}{CI_{red} - CI_{blue}}, \quad (4)$$

where  $CI(x)$  is the color index of the individual stars, and  $CI_{red}$ ,  $CI_{blue}$  are color indices for the fiducials of the red and the blue sequences of individual color indices, respectively (see also Milone et al. 2017). We derived fourth-order polynomial fits for individual color indices, and we show our parallelized CMDs and histograms in Figure 5. Note that our  $\|cn_{JWL}$  and  $\|cn'_{JWL}$  show discrete bimodal RGB distributions, a strong evidence of MPs in 47 Tuc. As we showed in Figure 4, our measurement uncertainties are significantly smaller than the widths of RGB sequences in individual color indices. Therefore, double RGB sequences in  $\|cn_{JWL}$

and  $\|cn'_{JWL}$  are thought to be real, reflecting a bimodal CN distribution of RGB stars in 47 Tuc (e.g., Hesser 1978; Norris & Freeman 1979; Briley et al. 1991; Lee 2019b). The  $\|m1$  and  $\|cy$  CMDs also suggest MPs in 47 Tuc, but the populational separations in the lower part of the RGB sequence are somewhat ambiguous as we already pointed out. We also note asymmetric distributions of RGB stars in the  $\|(b-y)$  and  $\|hk_{JWL}$ , extending toward smaller color index values, most likely due to the difference in metallicity in RGB stars in 47 Tuc as we will discuss below.

In our previous studies (Lee 2017, 2018, 2019a,c, 2020; Lee & Sneden 2021), we showed that both the  $cn_{JWL}$  and  $cn'_{JWL}$  indices are very powerful tools to classify MPs in GCs. As we already mentioned, our  $cn_{JWL}$  observations were limited to the central part of the cluster, and we decided to use the  $cn'_{JWL}$  to classify MPs in 47 Tuc in our current study. Assuming a bimodal  $\|cn'_{JWL}$  distribution as already shown in Figure 5, we applied the expectation maximization (EM) algorithm for a two-component Gaussian mixture model on our  $\|cn'_{JWL}$  index in order to perform a populational tagging

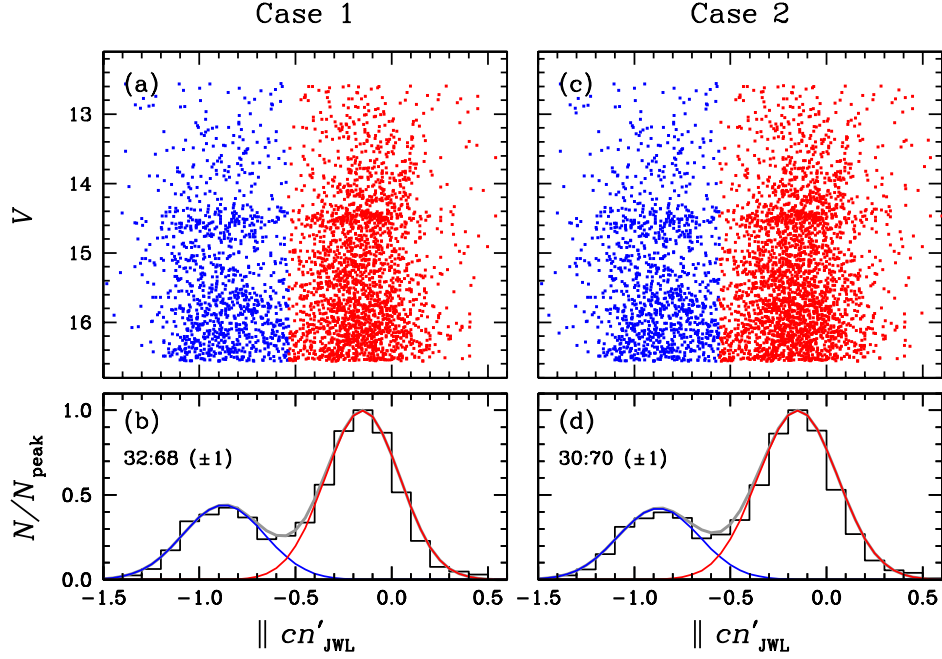


**Figure 6.** (a) A  $\|cn'_{JWL}\|$  vs.  $V$  CMD for the proper-motion member RGB stars (case (1)). The blue and red dots denote the CN-w and CN-s RGB stars in 47 Tuc returned from our EM estimator. (b) The black line denotes the  $\|cn'_{JWL}\|$  histogram of 47 Tuc RGB stars. The blue and red solid lines are the histograms returned from our EM estimator, and the gray solid line is for that of the total RGB population. (c) Same as (a) but for all RGB stars (case (2)). (d) Same as (b) but for all RGB stars.

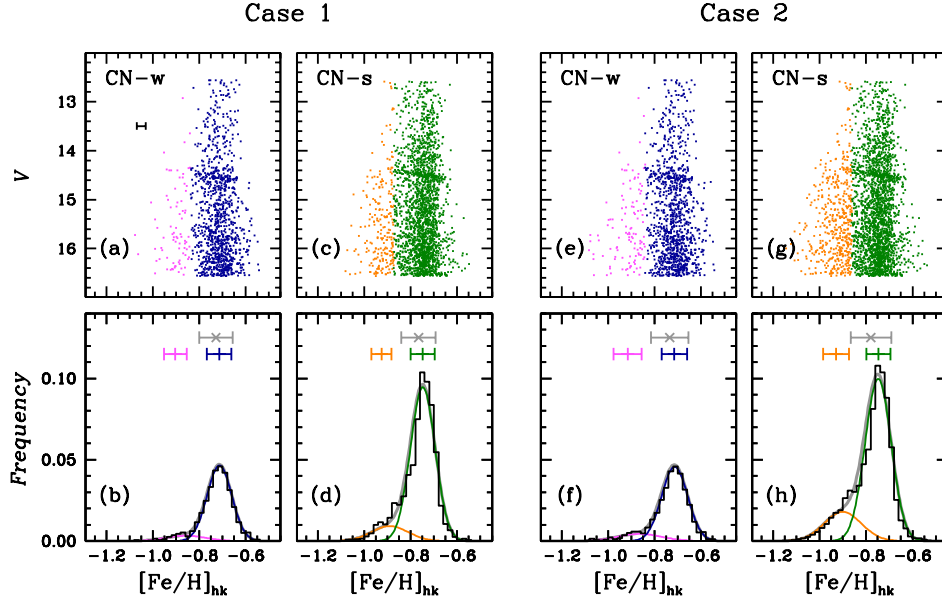


**Figure 7.** Metallicity distributions of individual populations. The pink, navy, orange, and dark-green colors denote the CN-w<sub>MP</sub>, CN-w<sub>MR</sub>, CN-s<sub>MP</sub>, and CN-s<sub>MR</sub>, respectively. Gray color denotes the whole population. The error bars are for  $\pm 1\sigma$ . In upper left corner of the panel (a), we show the measurement uncertainties ( $\pm 1\sigma$ ) using the bootstrap method,  $\pm 0.019$  dex.

**Table 1.** Abundances for input model atmospheres.

Element	Abundance	Note
[Fe/H]	-0.5, -0.7, -0.9	
$Y$	0.25, 0.28	
([C, N, O/Fe])	(0.00, 0.00, 0.30), (-0.30, 1.00, 0.00)	CNO1
	(0.15, 0.15, 0.50), (-0.45, 1.35, 0.10)	CNO2

of RGB stars in 47 Tuc. The stars with  $P(\|cn'_{JWL}|x_i) \geq 0.5$  from the EM estimator correspond to the CN-w population, where  $x_i$  denotes the individual RGB stars, while those with  $P(\|cn'_{JWL}|x_i) < 0.5$  correspond to the CN-s population. In an iterative manner, we calculated the probability of individual stars for being the CN-w and the CN-s populations. Through this process, we obtained the number ratio between the two populations  $n(\text{CN-w}):n(\text{CN-s}) = 32:68 (\pm 1)$  for the proper-motion member RGB stars (case (1)) and  $30:70 (\pm 1)$  for all RGB stars (case (2)). We show our result in Figure 6. As we will show later, the CN-s population is more centrally concentrated than the CN-w is, and the incomplete detection is more severe for the CN-s stars in the central part of cluster, resulting in a slightly smaller CN-s fraction when the proper-motion-selected RGB stars were used. Note that our result is significantly different from that of Milone et al. (2017). They relied on the HST photometry with a small FOV,  $\sim 3' \times 3'$ , compared to our observation,  $\sim 1^\circ \times 1^\circ$ , and they obtained  $N_1/N_{\text{tot}} = 0.175 \pm 0.009$ , where the  $N_1$  denotes the number of the FG of stars.

We emphasize that the FG of stars defined by Milone et al. (2017) is corresponding to our CN-w population (see Lee 2017). The discrepancy between our result and that of Milone et al. (2017) is a natural consequence of a small FOV of the HST observations of Milone et al. (2017) with a strong populational radial gradient in 47 Tuc. We note that Milone et al. (2012) obtained  $\sim 30\%$  of the FG of stars by combining the ground-based observations with a large FOV, consistent with our results.

## 6.2. Metallicity Distributions

As we mentioned earlier, our  $hk_{JWL}$  index is an excellent measure of the Ca II H & K lines (see Anthony-Twarog et al. 1991; Lee et al. 2009; Lee 2015, and references therein). Providing a constant [Ca/Fe] value in a given GC (e.g., Carney 1996; Marino et al. 2019), the  $hk_{JWL}$  index can be a good measure of metallicity. In our previous studies, we obtained the [Fe/H] values of individual RGB stars in M3 and M5 using our  $hk_{JWL}$  (Lee & Sneden 2021; Lee 2021). Here, we applied same procedure to derive metallicities of individual RGB stars in 47 Tuc.

To derive photometric metallicity of individual RGB stars, we used three different model isochrones, the Dartmouth (Dotter et al. 2008), PGPUC (Valcaroe et al. 2012), and  $Y^2$  (Yi et al. 2008). We obtained model grids for [Fe/H] = -0.9,

-0.7, and -0.5 dex with  $[\alpha/\text{Fe}] = +0.3$  dex,  $Y = 0.25$  and 0.28, and the age of 12 Gyr (e.g., see Brogaard et al. 2017). We constructed series of model atmospheres and synthetic spectra using ATLAS12 and SYNTHE (Kurucz 2011). During our calculations, we adopted two sets of CNO abundances between the CN-w and CN-s populations to explore how the CNO abundances may affect our results. For one set, we adopted ([C/Fe], [N/Fe], [O/Fe]) of (0.00, 0.00, 0.30) for the CN-w and (-0.30, 1.00, 0.00) for the CN-s (CNO1, see Table 1). For the other, we adopted (0.15, 0.15, 0.50) for the CN-w and (-0.45, 1.35, 0.10) for the CN-s (CNO2). Individual synthetic spectra were convolved with our filter transmission functions to be converted to our photometric system. Finally we calculated bolometric corrections for individual colors using the same method described by Girardi et al. (2002).

The photometric metallicity of individual RGB stars can be calculated using the following relation (e.g., see Lee & Sneden 2021);

$$[\text{Fe}/\text{H}]_{hk} \approx f(hk_{JWL}, M_V), \quad (5)$$

and we show our results in Table 2. We obtained the mean photometric metallicity of  $\langle [\text{Fe}/\text{H}]_{hk} \rangle \approx -0.75$  dex for 47 Tuc, and our result is consistent with that of previous results by others (e.g., see Carretta et al. 2009; Codero et al. 2014; Marino et al. 2016) to within measurement uncertainties. Not surprisingly, the metallicity from the proper-motion member RGB stars (case (1)) and that from all RGB stars (case (2)) are in excellent agreement. As shown in Tables 2 and 3, the differences in the photometric metallicity returned from different model isochrones are too small to affect our results,  $\Delta[\text{Fe}/\text{H}] \leq 0.02$  dex. We would like to emphasize that we are interested in the relative [Fe/H] values among RGB stars, and the differences in the relative [Fe/H] distributions from different model isochrones are negligibly small. Also importantly, the differences in metallicity from different CNO abundances are also negligibly small. In Table 4, we show  $\Delta[\text{Fe}/\text{H}]$  between those returned from the CNO1 and CNO2 compositions. We obtained the metallicity difference of  $\Delta[\text{Fe}/\text{H}] \leq 0.01$  dex, which may imply that the metallicity spread in 47 Tuc RGB stars described below may not be related to our adopted CNO abundances of individual populations. In the following analysis, we will take the  $[\text{Fe}/\text{H}]_{hk}$  returned from the Dartmouth isochrones as our reference photometric metallicity in order to maintain consistency with our previous works on M3 and M5 (Lee & Sneden 2021; Lee 2021). We emphasize again that the choice of our reference values does not affect our results.

In Figure 7, we show the metallicity distributions for the CN-w and CN-s populations. As already shown, there is no metallicity difference between the CN-w and CN-s populations, same as in our previous results for M3 and M5 (Lee & Sneden 2021; Lee 2021). On the other hand, both the CN-w and CN-s populations exhibit asymmetric metallicity distributions with long metal-poor tails, suggestive of multimodal metallicity distributions. We estimated measurement uncertainties using the bootstrap method, and we obtained  $\pm 0.019$  dex for both populations. As shown in Fig-



**Table 2.** Mean [Fe/H] values.

	Dartmouth $\langle[\text{Fe}/\text{H}]_{hk}\rangle$	$Y^2$ $\langle[\text{Fe}/\text{H}]_{hk}\rangle$	PGPUC $\langle[\text{Fe}/\text{H}]_{hk}\rangle$	Freq. (%)
Case (1): Proper-motion member (Gaia EDR3)				
Mean	$-0.753 \pm 0.075 \pm 0.001$	$-0.734 \pm 0.074 \pm 0.001$	$-0.730 \pm 0.074 \pm 0.001$	
CN-w	$-0.728 \pm 0.072 \pm 0.002$	$-0.731 \pm 0.073 \pm 0.002$	$-0.719 \pm 0.073 \pm 0.002$	32.3
CN-w <sub>MP</sub>	$-0.903 \pm 0.049 \pm 0.005$	$-0.900 \pm 0.046 \pm 0.005$	$-0.901 \pm 0.049 \pm 0.006$	2.3
CN-w <sub>MR</sub>	$-0.714 \pm 0.053 \pm 0.002$	$-0.717 \pm 0.055 \pm 0.002$	$-0.705 \pm 0.053 \pm 0.002$	30.0
CN-s	$-0.766 \pm 0.074 \pm 0.002$	$-0.736 \pm 0.074 \pm 0.002$	$-0.735 \pm 0.075 \pm 0.002$	67.7
CN-s <sub>MP</sub>	$-0.936 \pm 0.044 \pm 0.003$	$-0.911 \pm 0.037 \pm 0.003$	$-0.914 \pm 0.040 \pm 0.003$	6.6
CN-s <sub>MR</sub>	$-0.748 \pm 0.052 \pm 0.001$	$-0.723 \pm 0.058 \pm 0.001$	$-0.722 \pm 0.057 \pm 0.001$	61.1
Case (2): All RGBs				
Mean	$-0.766 \pm 0.088 \pm 0.001$	$-0.746 \pm 0.085 \pm 0.001$	$-0.742 \pm 0.087 \pm 0.001$	
CN-w	$-0.735 \pm 0.081 \pm 0.002$	$-0.738 \pm 0.082 \pm 0.002$	$-0.726 \pm 0.083 \pm 0.002$	29.7
CN-w <sub>MP</sub>	$-0.916 \pm 0.060 \pm 0.006$	$-0.911 \pm 0.055 \pm 0.005$	$-0.915 \pm 0.060 \pm 0.006$	2.8
CN-w <sub>MR</sub>	$-0.715 \pm 0.055 \pm 0.002$	$-0.717 \pm 0.057 \pm 0.002$	$-0.706 \pm 0.056 \pm 0.002$	26.9
CN-s	$-0.779 \pm 0.087 \pm 0.002$	$-0.749 \pm 0.086 \pm 0.002$	$-0.749 \pm 0.088 \pm 0.002$	70.3
CN-s <sub>MP</sub>	$-0.929 \pm 0.055 \pm 0.003$	$-0.913 \pm 0.048 \pm 0.003$	$-0.916 \pm 0.052 \pm 0.003$	9.8
CN-s <sub>MR</sub>	$-0.747 \pm 0.052 \pm 0.001$	$-0.724 \pm 0.058 \pm 0.001$	$-0.722 \pm 0.057 \pm 0.001$	60.5

**Table 3.** Differences in Mean [Fe/H] Values Using Different Isochrones.

	$\Delta\langle[\text{Fe}/\text{H}]\rangle$
$\Delta[\text{Fe}/\text{H}]_{hk}(\text{Dartmouth} - Y^2)$	$0.003 \pm 0.008 \pm 0.000$
$\Delta[\text{Fe}/\text{H}]_{hk}(\text{Dartmouth} - \text{PGPUC})$	$-0.020 \pm 0.012 \pm 0.000$
$\Delta[\text{Fe}/\text{H}]_{hk}(Y^2 - \text{PGPUC})$	$-0.006 \pm 0.008 \pm 0.000$

ure 7, our estimated measurement error is too small to fully explain the metallicity spread seen in each population, and we believe that the intrinsic metallicity differences among constituent stars are responsible for the asymmetric metallicity distributions. In order to examine multimodal metallicity distributions of 47 Tuc, we applied an EM analysis with a two-component Gaussian mixture model for the metallicity distributions of both the CN-w and CN-s populations. We show our results in Table 2 and Figure 7, suggesting that each population can be well described by bimodal metallicity distributions, reminiscent of M3 (Lee & Sneden 2021). The metal poor components (the CN-w<sub>MP</sub> and CN-s<sub>MP</sub>), which constitute about 10 – 13% of the total RGB population, are

about 0.2 dex more metal-poor than the metal-rich components (the CN-w<sub>MR</sub> and CN-s<sub>MR</sub>).

The *UBVI* photometry of Stetson et al. (2019) appears to support our results that 47 Tuc contains metal-poor components. In Figure 8, we show the  $(B-V)$ ,  $(B-I)$ , and  $(U-V)$  CMDs with three different radial zones,  $60'' \leq r < 200''$  (zone (1)),  $200'' \leq r < 400''$  (zone (2)), and  $400'' \leq r < 600''$  (zone (3)), in 47 Tuc. Note that only the *V* passband is not affected by the carbon and nitrogen abundance variations. Other photometric passbands, *U*, *B*, and *I* contain CN and CH molecular bands, and therefore, their magnitudes can be altered depending on their CNO abundances (i.e., the CN-w and CN-s). Interestingly, *B* passband contains both the CN and CH bands (see Figure 1 of Lee 2019c). In GC stars, where the carbon and nitrogen abundances are anticorrelated, the contribution of the CN molecules tends to be canceled out by that of the CH molecules (see also Sbordone et al. 2011). Therefore,  $(B-V)$  color is almost unaffected by the carbon and nitrogen abundance variations. In Figure 8, one can find that the  $(B-V)$  colors of the model isochrone for the CN-w<sub>MP</sub> are almost identical to those of the CN-s<sub>MP</sub>. The same is true for the CN-w<sub>MR</sub> and CN-s<sub>MR</sub>. The figure suggests that 47 Tuc contains metal-poor population in the central part of the cluster with a radial gradient, supporting our results discussed above.

**Table 4.** Differences in Mean [Fe/H] Values Using Different CNO Abundances.

	$\langle [\text{Fe}/\text{H}]_{\text{CNO1}} - [\text{Fe}/\text{H}]_{\text{CNO2}} \rangle$		
	All	CN-w	CN-s
Dartmouth	$-0.003 \pm 0.007 \pm 0.000$	$0.006 \pm 0.002 \pm 0.000$	$-0.007 \pm 0.008 \pm 0.000$
PGPUC	$-0.003 \pm 0.006 \pm 0.000$	$0.006 \pm 0.002 \pm 0.000$	$-0.007 \pm 0.008 \pm 0.000$
YAPSI	$-0.003 \pm 0.007 \pm 0.000$	$0.007 \pm 0.001 \pm 0.000$	$-0.008 \pm 0.009 \pm 0.000$

**Table 5.** RGBB  $V$  magnitudes.

Pop.	This Study	Stetson et al. (2019)
CN-w <sub>MP</sub>	14.399 ( $\pm 0.040$ )	14.408 ( $\pm 0.040$ )
CN-w <sub>MR</sub>	14.559 ( $\pm 0.025$ )	14.530 ( $\pm 0.025$ )
CN-s <sub>MP</sub>	14.385 ( $\pm 0.035$ )	14.358 ( $\pm 0.030$ )
CN-s <sub>MR</sub>	14.492 ( $\pm 0.020$ )	14.525 ( $\pm 0.020$ )

In Figure 9, we show comparisons of individual parallelized color indices of the proper-motion membership RGB stars in 47 Tuc. The figure clearly suggests that the four groups of stars that we obtained are truly separate populations occupying their own characteristic domains.

### 6.3. Red Giant Branch Bumps

During the course of low-mass star evolution, RGB stars experience a temporary drop in luminosity when the very thin H-burning shell crosses the discontinuity in the chemical composition and lowered mean molecular weight left by the deepest penetration of the convective envelope during the ascent of the RGB. RGB stars in such evolutionary phases have to cross three times the same luminosity interval, leaving a distinctive feature, the so-called RGBB (e.g., see Renzini & Fusi Pecci 1988; Cassisi & Salaris 2013). It is well recognized that, at a given age, the RGBB luminosity increases with helium abundance and decreases with metallicity (e.g., see Cassisi & Salaris 1997). Accurate differential photometry can be possible in the GC MP study, and therefore, one can precisely estimate relative helium contents among MPs in a given GC with prior metallicity information (e.g., see Bragaglia et al. 2010; Lee 2015, 2017, 2018; Milone et al. 2018b; Lagioia et al. 2018; Lee & Sneden 2021).

In order to derive the RGBB  $V$  magnitudes, we calculated the generalized differential luminosity functions (LFs) using a Gaussian kernel density estimation for individual populations in 47 Tuc. We determined the peak values as our RGBB  $V$  magnitudes for individual populations. In Figure 10 and Table 5, we show our results, obtaining the RGBB  $V$  magnitudes of 14.399 ( $\pm 0.040$ ), 14.559 ( $\pm 0.025$ ), 14.385 ( $\pm 0.035$ ), 14.492 ( $\pm 0.020$ ) mag for the CN-w<sub>MP</sub>, CN-w<sub>MR</sub>, CN-s<sub>MP</sub>, and CN-s<sub>MR</sub>, respectively. We caution that the num-

ber of RGBB stars, in particular, for the CN-w<sub>MP</sub> population is very small and it is worrisome that our RGBB  $V$  magnitude may not be accurate.

We applied the same procedures for the  $UBVRI$  photometry by Stetson et al. (2019), to see if their data show the same trend in the RGBB  $V$  magnitudes. First, we select the proper-motion member stars using the Gaia EDR3. Then we separated the CN-w and CN-s populations using the  $\Delta C_{UBI}$  index,

$$\Delta C_{UBI} = \frac{C_{UBI} - C_{UBI,r}}{C_{UBI,r} - C_{UBI,b}}, \quad (6)$$

where  $C_{UBI} = (U - B) - (B - I)$ , while  $C_{UBI,b}$  and  $C_{UBI,r}$  denote the fiducials for the  $C_{UBI}$ -blue and  $C_{UBI}$ -red sequences, respectively, at a given magnitude (Milone et al. 2012; Lee 2019a). To perform a populational tagging, we applied the EM algorithms for a two-component Gaussian mixture model. Through this process, we obtained populational number ratio of  $n(\text{CN-w}):n(\text{CN-s}) = 32:68 (\pm 1)$ , consistent with our result based on the proper-motion member stars. As already shown in Figure 8, the  $(B - V)$  color depends more sensitively on metallicities than the helium abundances or the variations in the CNO abundances (also see, Sbordone et al. 2011). Therefore, the  $(B - V)$  color can be used as a metallicity indicator. We calculated the  $(B - V)$  color difference between individual RGB stars and the mean  $(B - V)$  fiducial sequence,  $\Delta(B - V)$ , which shows asymmetric distributions toward the small  $(B - V)$  values for both populations. We performed the populational tagging for the CN-w and CN-s populations by applying the EM algorithm for a two-component Gaussian mixture model on the  $\Delta(B - V)$  distributions. We obtained  $\Delta(B - V)_{\text{blue}} : \Delta(B - V)_{\text{red}} = 6:94 (\pm 2)$  for the CN-w population and  $9:91 (\pm 2)$  for the CN-s population, where  $\Delta(B - V)_{\text{blue}}$  and  $\Delta(B - V)_{\text{red}}$  denote RGB stars bluer or redder than the mean fiducial sequence at a given  $V$  magnitude. We note that these values are consistent with those presented in Table 2 using our own photometry. Given the similar populational number ratios and the metallicity sensitivity of the  $(B - V)$  color, we argue that  $\Delta(B - V)_{\text{blue}}$  and  $\Delta(B - V)_{\text{red}}$  are corresponding to the metal-poor and metal-rich subpopulations in the CN-w and CN-s populations, respectively. We calculated generalized differential LFs using a Gaussian kernel density estimation for the photometry by Stetson et al. (2019) and we obtained the RGBB  $V$  magnitudes of 14.408 ( $\pm 0.040$ ), 14.530 ( $\pm 0.025$ ), 14.358 ( $\pm 0.030$ ), 14.525 ( $\pm 0.020$ ) mag for the CN-w<sub>MP</sub>, CN-w<sub>MR</sub>, CN-s<sub>MP</sub>, and CN-s<sub>MR</sub>. We show our results in Fig-

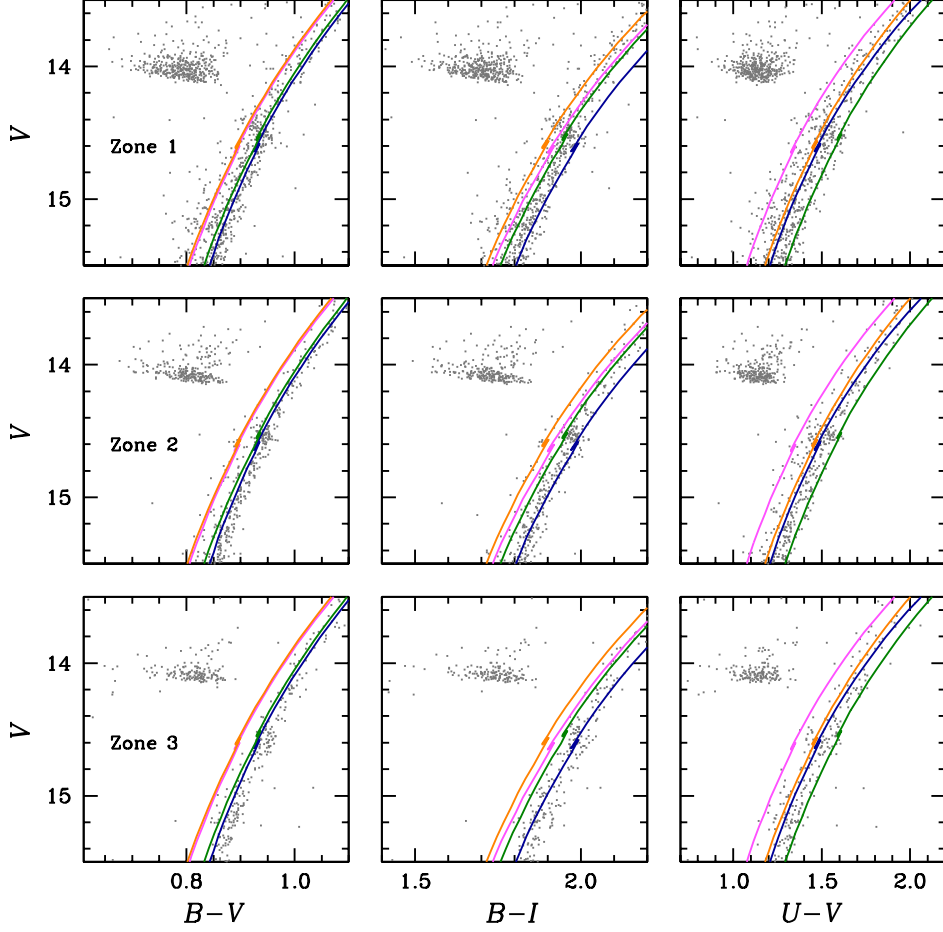


**Figure 8.** The  $(B-V)$ ,  $(B-I)$ , and  $(U-V)$  CMDs using the multi-color photometry of Stetson et al. (2019) with three different radial zones,  $60'' \leq r < 200''$  (zone (1)),  $200'' \leq r < 400''$  (zone (2)), and  $400'' \leq r < 600''$  (zone (3)), in 47 Tuc. Note that we used stars with low photometric measurement uncertainties,  $\sigma(B-V) \leq 0.01$  mag. The pink, navy, orange, and dark-green colors denote model isochrones with  $([\text{Fe}/\text{H}], Y, \text{CNO}) = (-0.90 \text{ dex}, 0.25, \text{CN-w}), (-0.70 \text{ dex}, 0.25, \text{CN-w}), (-0.90 \text{ dex}, 0.25, \text{CN-s}),$  and  $(-0.70 \text{ dex}, 0.28, \text{CN-s})$ , respectively, for 12 Gyr.

ure 11 and Table 5. We emphasize that the RGBB  $V$  magnitudes of individual populations using the photometric data by Stetson et al. (2019) are in good agreement with those from our results. The number of RGBB stars of the CN- $w_{\text{MP}}$  population of Stetson et al. (2019) is still small, but it is strongly believed that the RGBB at  $V \sim 14.40$  mag for the CN- $w_{\text{MP}}$  population is a real feature.

In order to derive the relative helium abundances and metallicities, we compare our RGBB  $V$  magnitudes with those from model isochrones. In Figure 12, we show plots of the  $V_{\text{bump}}$  and  $(V_{\text{bump}} - V_{\text{TO}})$  against  $[\text{Fe}/\text{H}]$  for model isochrones with  $Y = 0.250$  (0.257), 0.275, and 0.300. We used three different isochrones currently available:  $Y^2$  (Yi et al. 2008), the PGPUC (Valcarce et al. 2012), and the Bag of Stellar Tracks and Isochrones (BaSTI; Pietrinferni et al. 2021). To determine the  $V_{\text{bump}}$  of individual model isochrones, we performed Monte Carlo simulations by constructing evolutionary population synthesis models, sim-

ilar to those of our previous studies (e.g., see Lee & Sneden 2021, and references therein), with various metallicity and helium contents. We populated 200,000 artificial stars for individual model isochrones with different chemical abundances, and we generated generalized histograms to derive the  $V_{\text{bump}}$  as we did for our observed data. We note that the  $V_{\text{bump}}$  of each model isochrone is brighter than our observations. Therefore, we subtracted 0.17, 0.22 and 0.28 mag from the  $V_{\text{bump}}$  of the  $Y^2$ , PGPUC and BaSTI model isochrones, respectively, to match observed  $[\text{Fe}/\text{H}]$ ,  $\sim -0.72$  dex, and presumed helium abundance,  $Y \sim 0.25$ , for the CN- $w_{\text{MR}}(\text{RGB})$  population (see also, Lee 2015; Lee & Sneden 2021, for the discrepancies in the RGBB magnitudes in model isochrones). In Table 6, we show the results for the  $V_{\text{bump}}$  and  $V_{\text{bump}} - V_{\text{TO}}$  dependencies on  $[\text{Fe}/\text{H}]$  and  $Y$ . The difference in the RGBB  $V$  magnitude of  $0.067(\pm 0.032)$  mag between the CN- $w_{\text{MR}}$  and CN- $w_{\text{MP}}$  can be translated into the helium abundance difference of  $\Delta Y = 0.029(\pm 0.014)$ ,

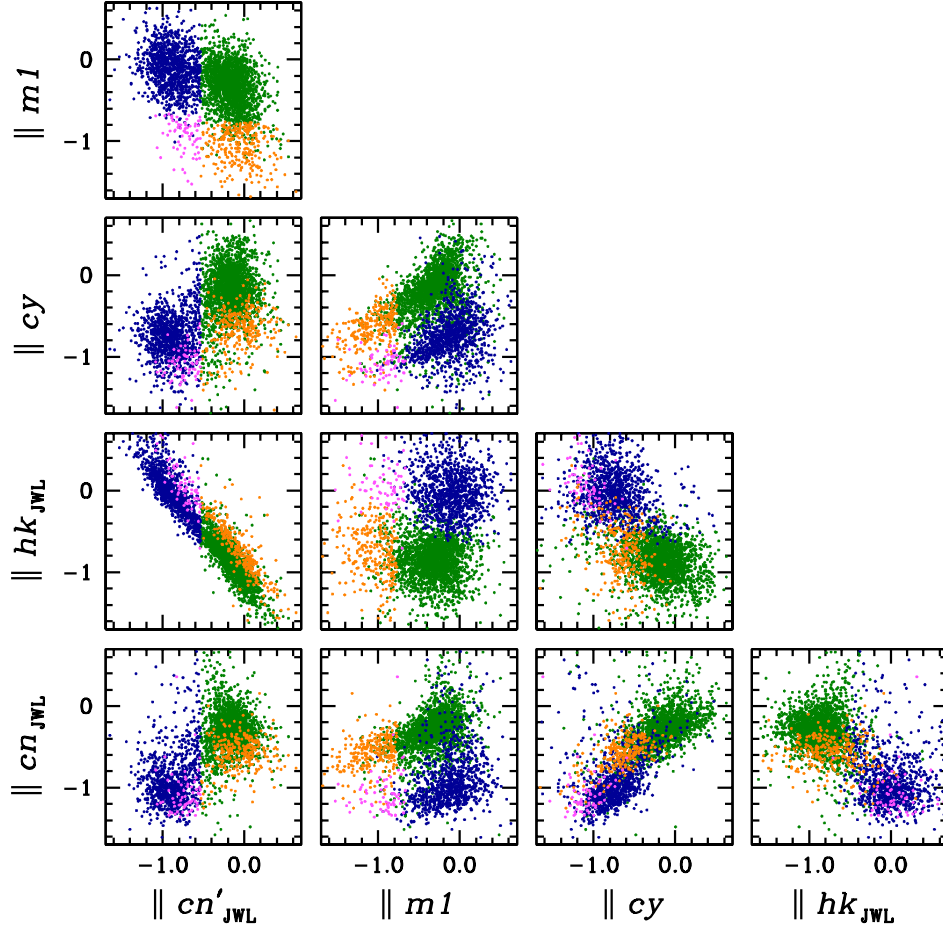


**Figure 9.** Comparisons of parallelized color indices of the proper-motion membership 47 Tuc RGB stars with  $-1.5 \leq V - V_{\text{HB}} \leq 2.5$  mag, showing that our four groups of stars are different stellar populations. Colors are the same as Figure 7.

0.028( $\pm 0.013$ ) and 0.043( $\pm 0.021$ ) from relation (1) in Table 6 using the  $Y^2$ , PGPUC and BaSTI isochrones, respectively. Note that the result from the BaSTI model isochrone is larger than the other two isochrones.

Due to the well-known discrepancy between theory and observations concerning the RGBB brightness, it was kindly recommended by the referee that comparisons of the difference in brightness between the RGBB magnitude associated with the individual populations and the corresponding theoretical quantities would be more reasonable. In this respect, we obtained the turn-off  $V$  magnitude of 17.588( $\pm 0.020$ ) mag for 47 Tuc, and we calculated the ( $V_{\text{bump}} - V_{\text{TO}}$ ) of individual populations assuming they have the same turn-off magnitude. Note that this assumption may not be appropriate unless they have slightly different ages, since, at a given age, the turn-off  $V$  magnitude becomes brighter with decreasing metallicity and increasing helium abundance. Using relation (2) in Table 6, we obtained the helium abundance difference of  $\Delta Y = 0.016(\pm 0.008)$ ,  $0.017(\pm 0.008)$  and  $0.018(\pm 0.009)$  from the  $Y^2$ , PGPUC, and BaSTI isochrones, respectively. Note that all of three estimates provide consistent degrees of helium enhancement, but they are much smaller than those

from relation (1) above. Our estimates of helium abundance difference between the CN- $w_{\text{MR}}$  and CN- $s_{\text{MR}}$  are  $\Delta Y = 0.016 - 0.043$ , which are in good agreement with those of Anderson et al. (2009, for MS), Di Criscienzo et al. (2010, for SGB), and Nataf et al. (2011, for RGBB),  $\Delta Y \sim 0.03$ . On the other hand, the relative helium abundance estimates based on the HST observations of the RGBB by Milone et al. (2018b,  $\Delta Y = 0.011 \pm 0.005$ ) and Lagioia et al. (2018,  $\Delta Y = 0.010 \pm 0.004$ ) appear to be too small compared to our results, although their estimates are marginally agree with our results from relation (2) within the uncertainties.

We also attempt to calculate the metallicity difference between the CN- $w_{\text{MR}}$  and CN- $w_{\text{MP}}$  based on their RGBB  $V$  magnitudes. Using relation (3) in Table 6, we obtained 0.142( $\pm 0.042$ ), 0.131( $\pm 0.039$ ) and 0.154( $\pm 0.045$ ) from the  $Y^2$ , PGPUC and BaSTI isochrones, respectively, all of which are slightly smaller than the metallicity difference from our  $hk_{\text{JWL}}$  photometry. When we used relation (4), we obtained consistent results with that from the  $hk_{\text{JWL}}$  photometry, finding 0.197( $\pm 0.058$ ), 0.165( $\pm 0.048$ ) and 0.192( $\pm 0.057$ ) from the  $Y^2$ , PGPUC and BaSTI isochrones, respectively.



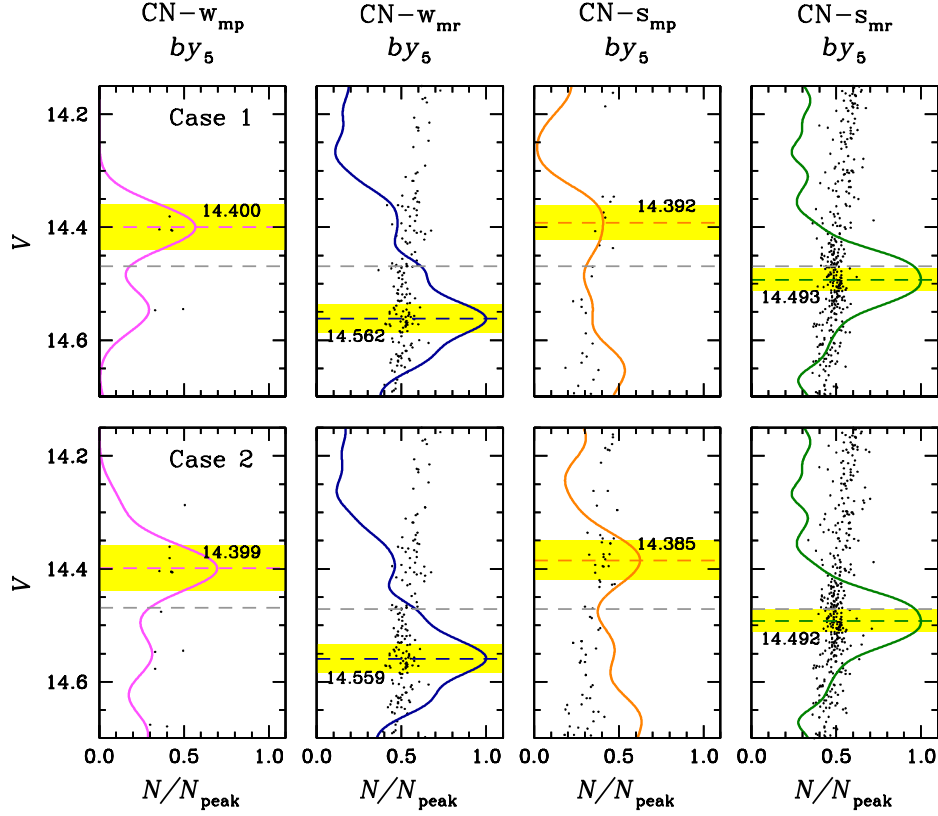


**Figure 10.** Plots of  $by_5$  vs.  $V$  CMDs and differential LFs of individual populations. We show the mean RGBB  $V$  magnitudes of individual populations with gray dotted lines and those of individual populations with dotted lines with respective colors and yellow-shaded boxes. Note that the  $by_5$  values are defined to be  $by_5 = 5 \times (b - y) - 2.5$  for the clarity of the figure.

As shown in Figures 10 and 11, the number of the CN-SMP RGB stars around the RGBB regime is greater than that of the CN-WMP, in particular for the case (2) (using the photometrically selected RGB stars). Therefore, it can be thought that using the CN-SMP RGBB  $V$  magnitude would be more reliable to estimate the metallicity difference between the metal-rich and metal-poor components. The RGBB  $V$  magnitude of the CN-SMP,  $V = 14.385(\pm 0.035)$ , can be interpreted in the following three ways:

1. The CN-SMP population has the same helium abundance as the CN-WMR but lower  $[\text{Fe}/\text{H}]$ .
2. The CN-SMP population has the same helium abundance as the CN-SMR but lower  $[\text{Fe}/\text{H}]$ .
3. The CN-SMP population has the same  $[\text{Fe}/\text{H}]$  as the CN-WMR and CN-SMR but enhanced helium abundance.

In case (1) above, we obtained that the CN-SMP population should be  $0.155(\pm 0.010, \text{relation (3)})$  and  $0.200(\pm 0.015, \text{relation (4)})$  dex lower than the CN-WMR. Not surprisingly, these are the similar metallicities that we derived for the CN-WMP. In case (2), the CN-SMP should be  $\Delta[\text{Fe}/\text{H}] = 0.095(\pm 0.006, \text{relation (3)})$  and  $0.123(\pm 0.009, \text{relation (4)})$

dex more metal-poor than the CN-SMR. Finally, in case (3), the CN-SMP should be  $\Delta Y = 0.086(\pm 0.017, \text{relation (1)})$  and  $0.044(\pm 0.002, \text{relation (2)})$  dex more helium enhanced than the CN-WMR.

As we will show below, the RHB morphology of 47 Tuc can be explained best by case (1), i.e., the CN-SMP RHB populations has the same helium abundance as the CN-WMR population and a lower metallicity by  $\Delta[\text{Fe}/\text{H}] \sim -0.20$  dex. Therefore, our results may suggest that both the CN-WMP and CN-SMP have the same metallicity and helium abundance.

#### 6.4. Cumulative Radial Distributions

The cumulative radial distributions (CRDs) of individual MPs may provide crucial information on the formation and dynamical evolution of MPs. Many previous studies on the formation of GCs with MPs suggested that the CN-s populations form in the innermost part of the cluster in a more extended CN-w system (e.g., see D'Ercole et al. 2008; Bekki 2019; Cassisi & Salaris 2021). Moreover, the degree of helium enhancement or the multiphase formations of the later generation of stars can be dependent on the external gas density (Calura et al. 2019). The initial structural difference between the CN-w and CN-s populations can be gradually erased with time, due to the result of the preferential loss of the CN-w stars during the cluster's dynamical evolution (e.g.,

**Table 6.** Slopes in  $V_{\text{bump}}$  magnitudes versus  $[\text{Fe}/\text{H}]$  and  $Y$ .

Relation ( $\Delta$ Abundance)	Slope $a$		
	$Y^2$	PGPUC	BaSTI
(1) $V_{\text{bump}} \propto a \times Y$ $\Delta Y^1$	$-2.279 \pm 0.028$ $0.029 \pm 0.014$	$-2.425 \pm 0.033$ $0.028 \pm 0.013$	$-1.571 \pm 0.134$ $0.043 \pm 0.021$
(2) $(V_{\text{bump}} - V_{\text{To}}) \propto a \times Y$ $\Delta Y^1$	$-4.267 \pm 0.163$ $0.016 \pm 0.008$	$-3.947 \pm 0.192$ $0.017 \pm 0.008$	$-3.790 \pm 0.504$ $0.018 \pm 0.009$
(3) $V_{\text{bump}} \propto a \times [\text{Fe}/\text{H}]$ $\Delta [\text{Fe}/\text{H}]^2$	$1.124 \pm 0.015$ $0.142 \pm 0.042$	$1.221 \pm 0.021$ $0.131 \pm 0.039$	$1.036 \pm 0.006$ $0.154 \pm 0.045$
(4) $(V_{\text{bump}} - V_{\text{To}}) \propto a \times [\text{Fe}/\text{H}]$ $\Delta [\text{Fe}/\text{H}]^2$	$0.814 \pm 0.019$ $0.197 \pm 0.058$	$0.972 \pm 0.017$ $0.165 \pm 0.048$	$0.835 \pm 0.036$ $0.192 \pm 0.057$

<sup>1</sup> The difference in helium abundance between the CN- $w_{\text{MR}}$  and CN- $s_{\text{MR}}$ .

<sup>2</sup> The difference in  $[\text{Fe}/\text{H}]$  between the CN- $w_{\text{MR}}$  and CN- $w_{\text{MP}}$ .

**Table 7.**  $p$  Values Returned from the K-S Tests for the CRDs of individual RGB populations

	CN-s	CN- $w_{\text{MP}}$	CN- $w_{\text{MR}}$	CN- $s_{\text{MP}}$	CN- $s_{\text{MR}}$
CN-w	$< 1.00 \times 10^{-15}$	$< 1.00 \times 10^{-15}$	0.234	$< 1.00 \times 10^{-15}$	$< 1.00 \times 10^{-15}$
CN-s		0.180	$< 1.00 \times 10^{-15}$	$< 1.00 \times 10^{-15}$	$1.88 \times 10^{-2}$
CN- $w_{\text{MP}}$			$< 1.00 \times 10^{-15}$	$2.80 \times 10^{-6}$	$3.21 \times 10^{-2}$
CN- $w_{\text{MR}}$				$< 1.00 \times 10^{-15}$	$< 1.00 \times 10^{-15}$
CN- $s_{\text{MP}}$					$< 1.00 \times 10^{-15}$

see [Vesperini et al. 2021](#)). It is also plausible that the current location can be affected by the stellar masses due to different degree of diffusion processes. For example, the later generations of stars with enhanced helium abundances have smaller stellar masses due to their fast evolution. Over the Hubble time, the radial distributions of the later generations of stars can expand outward (e.g., see [Fare et al. 2018](#); [Calura et al. 2019](#)).

In this context, we derive the CRDs of individual MPs in 47 Tuc, and we show our results in Figure 13. It is very interesting to note that the metal-poor components, the CN- $w_{\text{MP}}$  and CN- $s_{\text{MP}}$ , have significantly more centrally concentrated CRDs than the metal-rich components, the CN- $w_{\text{MR}}$  and CN- $s_{\text{MR}}$ , similar to those in M3 ([Lee & Sneden 2021](#)). Furthermore, the CN- $s_{\text{MP}}$  population is more centrally concentrated than the CN- $w_{\text{MP}}$  suggesting that the metal-poor populations mimic the general trend of normal GCs, i.e., the more centrally concentrated nature of the CN-s population. We performed the Kolmogorov–Smirnov (K-S) tests, and our results show that the CRDs of individual populations are statistically independent each other as shown in Table 7.

In the figure, we also show the fraction of the FG of stars (equivalent to our CN-w) from the HST photometry by [Milone et al. \(2017\)](#),  $0.175 \pm 0.009$ . Their FOV of HST observation was  $\sim 3' \times 3'$ , significantly smaller than that of our study,  $\sim 1^\circ \times 1^\circ$ . Due to a strong radial gradient of the populational ratio, it is most likely that [Milone et al. \(2017\)](#) underestimated the fraction of the FG of stars. We derived the fraction of the CN-w population within the radial distance of one half-light radius ( $\sim 3'.2$ ),  $0.159 \pm 0.013$ , and our result is consistent with that of [Milone et al. \(2017\)](#),  $0.175 \pm 0.009$ . Our exercise shows the importance of securing a large FOV when deriving populational number ratios of GCs with MPs.

### 6.5. Radial Abundance Gradients

Since the late 70s, it has been known that 47 Tuc shows the radial abundance and color gradients. For example, from their pioneering works, [Chun & Freeman \(1979\)](#), and [Norris & Freeman \(1979\)](#) found that the CN-s RGB stars are more centrally concentrated than the CN-w stars are. Using our  $cn'_{\text{JWL}}$  index, which is a measure of the CN band strengths at  $\lambda 3883$ , we examined radial variation of CN strengths. We

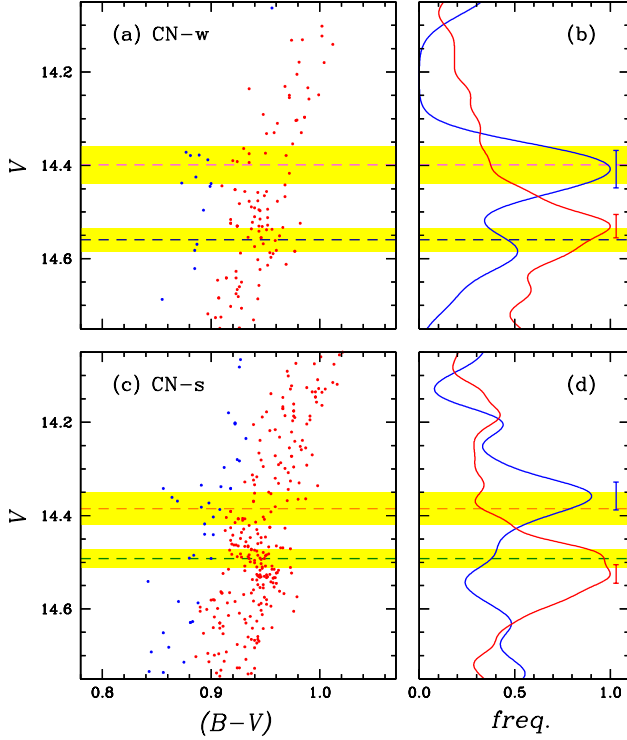


**Figure 11.** (a) Plots of  $(B-V)$  vs.  $V$  CMD for the CN-w population using the photometric data by Stetson et al. (2019). The blue and red dots denote the  $\text{CN-w}_{\text{MP}}$  and  $\text{CN-w}_{\text{MR}}$  stars based on the  $\parallel (B-V)$  distribution. The horizontal long-dashed lines and yellow boxes denote the  $V_{\text{bump}}$  and measurement uncertainties for the  $\text{CN-w}_{\text{MP}}$  (pink) and  $\text{CN-w}_{\text{MR}}$  (navy) populations based on our own photometry. (b) Differential LFs of the  $\text{CN-w}_{\text{MP}}$  (blue) and  $\text{CN-w}_{\text{MR}}$  (red). The error bars denote the measurement uncertainties using the data by Stetson et al. (2019). (c) Same as (a) but for the CN-s population. (d) Same as (b) but for the CN-s population.

calculated the moving average of the radially adjacent 50 RGB stars, and we show our results in Figure 14. The figure shows that the average  $cn'_{\text{JWL}}$  value is significantly larger, i.e., more CN-rich, in the central part of the cluster, and it decreases with radial distance up to about  $10'$ . This is consistent with the fact that the CN-s stars are more centrally concentrated as we already discussed earlier. When we use all RGB stars, which are photometrically selected and contain more complete samples in the central part of the cluster, the slope of the abundance gradient becomes steeper due to inclusion of more CN-s RGB stars in the central part of the cluster. Beyond the radial distance of  $10'$ , the  $cn'_{\text{JWL}}$  value maintains a constant level due to the domination of the CN-w population in the outer regime of the cluster.

We also investigated the radial  $[\text{Fe}/\text{H}]_{hk}$  variation of the cluster. As shown in Figure 14, the mean  $[\text{Fe}/\text{H}]_{hk}$  value is smaller in the central part, and then it increases with the radial distance up to about  $10'$  and maintains a constant level, consistent with the fact that the metal-poor stars are signifi-

cantly more centrally concentrated than the metal-rich stars, reminiscent of M3 (Lee & Sneden 2021). This is also supported by the  $(B-V)$  color gradient of 47 Tuc RGB stars as we showed in Figure 8.

## 7. RED HORIZONTAL BRANCH

Since the GC RHB stars are not warm enough to completely suppress the formation of diatomic molecules, such as NH, CN, and CH, in their surface, our color indices can be useful to perform populational tagging for RHB stars (Lee & Sneden 2021, and references therein). In their pioneering work, Norris & Freeman (1982) studied RHB in 47 Tuc, finding the CN-s RHB stars are enhanced in nitrogen by  $\Delta[\text{N}/\text{Fe}] \approx 0.9$  dex and depleted in carbon by  $\Delta[\text{C}/\text{Fe}] \approx 0.3$  dex with respect to the CN-w RHB stars. They also argued the  $V$  magnitude difference of 0.04 mag between the two RHB groups, and they attributed it to difference in helium abundance.

Here, we investigate the RHB population in 47 Tuc using our color indices, finding that differences not only in helium abundance but also in metallicity are necessary to explain the observed RHB CMDs.

### 7.1. Populational Tagging

In Figure 15(a), we show a plot of the  $[\text{O}/\text{Fe}]$  versus  $[\text{Na}/\text{Fe}]$  of the RHB stars in 47 Tuc (Gratton et al. 2013). In the figure, the blue- and red-filled circles denote the RHB stars with  $[\text{Na}/\text{O}] \leq 0.2$  dex (the Na-normal and equivalent to the CN-w) and  $> 0.2$  dex (the Na-enhanced and equivalent to the CN-s), respectively. In panel (b), we show a plot of  $hk_{\text{JWL}}$  versus  $cn'_{\text{JWL}}$  for the RHB stars in 47 Tuc. At the given  $hk_{\text{JWL}}$  values, our  $cn'_{\text{JWL}}$  index is well correlated with the sodium abundance, due to the existence of a correlation between the CN and the sodium abundances, confirming our previous result that our  $cn_{\text{JWL}}$  and  $cn'_{\text{JWL}}$  indices can be a powerful tool to investigate the MP of the RHB stars. In the figure, the  $cn'_{\text{JWL}}$  gradient against the  $hk_{\text{JWL}}$  is partially due to the temperature effect along the RHB, in a sense that as the effective temperature of RHB stars increases the suppression of the CN band at  $\lambda 3883$  becomes greater resulting in small  $cn'_{\text{JWL}}$  values. When the effective temperature increases even higher, the influence of the  $\text{H}_{\zeta}$  and  $\text{H}_{\eta}$  at  $3889.05$  and  $3835.38\text{\AA}$  becomes important, resulting in larger  $cn'_{\text{JWL}}$  values with temperatures as can be seen in the M3 RHB stars (e.g., see Lee & Sneden 2021).

We performed the populational tagging of the RHB stars in 47 Tuc using the similar method that we applied for the RGB stars. In Figure 16(a), we show a plot of  $hk_{\text{JWL}}$  versus  $cn'_{\text{JWL}}$  of the RHB stars in 47 Tuc. We set a boundary between the two groups of the RHB stars and rotate the  $hk_{\text{JWL}}$  versus  $cn'_{\text{JWL}}$  plane so that the boundary line becomes parallel to the vertical axis as shown in Figure 16(b). Then we applied the EM analysis with a Gaussian mixture models along the  $x$ -axis, which is perpendicular to the boundary line. Through this process, we obtained the populational number ratio of  $n(\text{CN-w}):n(\text{CN-s}) = 30:70 (\pm 2)$ , consistent with that of RGB. Note that our result does not agree with those of Milone et al.

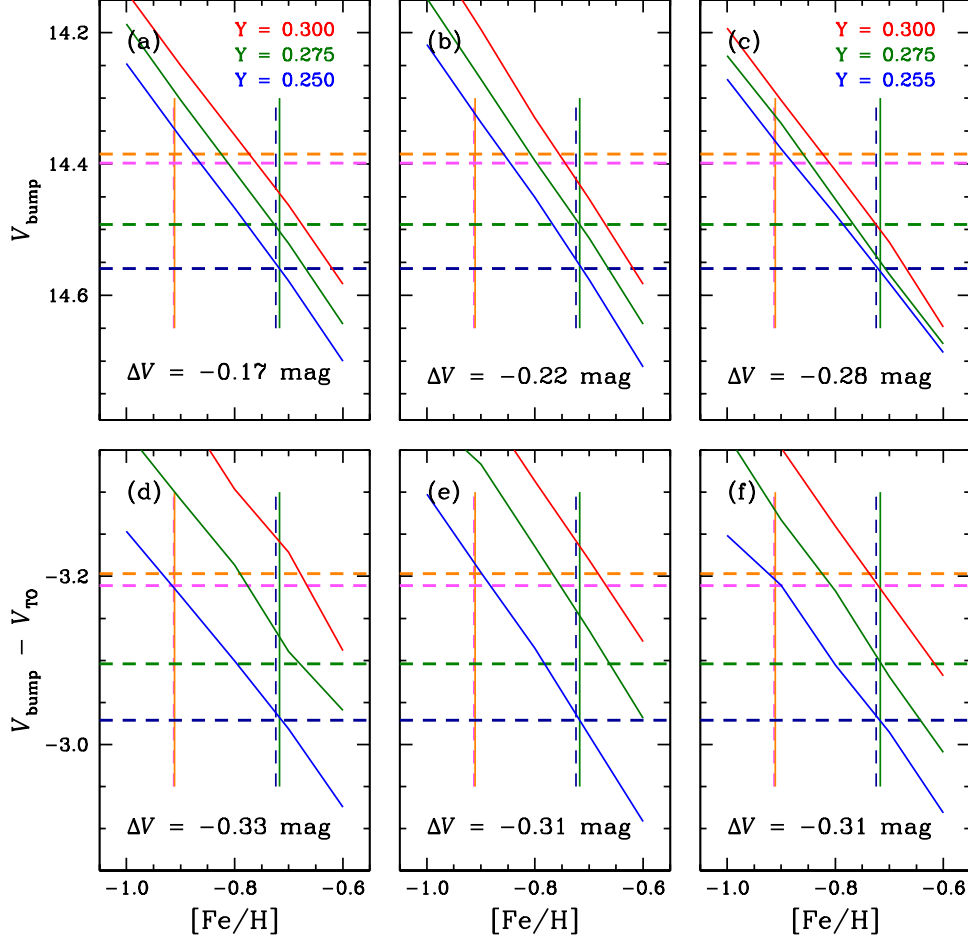


**Figure 12.** (a) A plot of  $V_{\text{bump}}$  versus  $[\text{Fe}/\text{H}]$  using the  $Y^2$  isochrones for  $Y = 0.250, 0.275$ , and  $0.300$  along with those of four populations in 47 Tuc. The  $\Delta V$  indicates the  $V$  magnitude offset in model isochrones to match our  $V_{\text{bump}}$  magnitude the CN-wMR population. The colors are the same as Figure 7. (b) Same as (a) but using the PGPUC isochrones. (c) A plot of  $V_{\text{bump}}$  versus  $[\text{Fe}/\text{H}]$  using the BaSTI isochrones for  $Y = 0.255, 0.275$ , and  $0.300$ . (d) A plot of  $(V_{\text{bump}} - V_{\text{TO}})$  versus  $[\text{Fe}/\text{H}]$  using the  $Y^2$  isochrones. (e) Same as (d) but using the PGPUC isochrones. (f) Same as (d) but using the BaSTI isochrones.

(2012) or Dondoglio et al. (2021), who employed the HST photometry and obtained  $n(\text{CN-w}):n(\text{CN-s}) \sim 20:80$ . Again, their results are based on the central part of the cluster owing to the small FOV of the HST observations. Therefore, it is natural to have a larger fraction ( $\sim 80\%$ ) of the CN-s population due to a strong radial populational gradient of 47 Tuc.

We also examined the  $y$  distributions of each RHB population. As shown in Figure 16(d), the  $y$  range of the CN-s(RHB) appears to be very large compared to that of the CN-w(RHB). Moreover, the  $y$  distribution of the CN-s(RHB) exhibits an asymmetric distribution, suggesting that the CN-s(RHB) may contain multiple subpopulations as can be seen in the RGB stars. Assuming a bimodal distribution of the CN-s(RHB) population, we applied the EM analysis with a two-component Gaussian mixture model along the  $y$ -axis for the CN-s(RHB) stars. We obtained the populational number ratio of  $n[\text{CN-s}_{\text{MP}}(\text{RHB})]:n[\text{CN-s}_{\text{MR}}(\text{RHB})] = 10:90 (\pm 2)$ , where the CN-s<sub>MP</sub>(RHB) and CN-s<sub>MR</sub>(RHB) refer the CN-

s RHB stars with high and low  $y$  values, respectively. We note that the  $y$ -axis is roughly the inverse of the  $hk_{\text{JWL}}$  index. Therefore, the CN-s<sub>MP</sub>(RHB) stars are those with smaller  $hk_{\text{JWL}}$ , the photometric measure of the metallicity at a given effective temperature in the RHB temperature range. Also it will be shown below that the CN-s<sub>MP</sub>(RHB) population can be explained best with the lower metallicity by  $\Delta[\text{Fe}/\text{H}] \sim -0.2$  dex as can be seen in the RGB populations.

We show  $(b-y)$  CMDs of the 47 Tuc RHB stars in Figure 17 along with the BaSTI models (Pietrinferni et al. 2021), by using the distance modulus of  $(m-M)_0 = 13.21$  mag and the interstellar reddening of  $E(B-V) = 0.03$  mag (Brogaard et al. 2017). The HB isochrones with constant mass loss for  $([\text{Fe}/\text{H}], Y, \text{age}) = (-0.7, 0.257, 12.0 \text{ Gyr})$ ,  $(-0.7, 0.275, 12.0 \text{ Gyr})$ , and  $(-0.9, 0.257, 12.0 \text{ Gyr})$  can nicely explain the color and magnitude distributions of the CN-w(RHB), CN-s<sub>MR</sub>(RHB) and CN-s<sub>MP</sub>(RHB), respectively. We note that the CN-s<sub>MP</sub>(RHB) occupies about 7



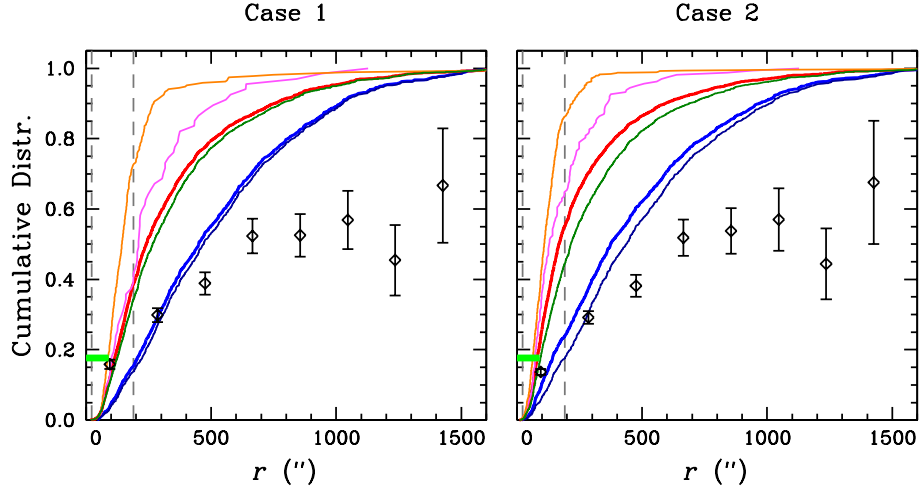


**Figure 13.** CRDs of individual RGB populations. Colors for individual populations are the same as Figures 7 and 9, while the thick blue and red solid lines denote the whole CN-w and CN-s populations. The error bars show the fraction of the CN-w population with a binning radial distance of the half-light radius. The vertical gray dashed lines denote the core and the half-light radii of 47 Tuc. The green-shaded box indicates the fraction of the first generation by Milone et al. (2017),  $0.175 \pm 0.009$ , measured in the central part of the cluster,  $\sim 3' \times 3'$ .

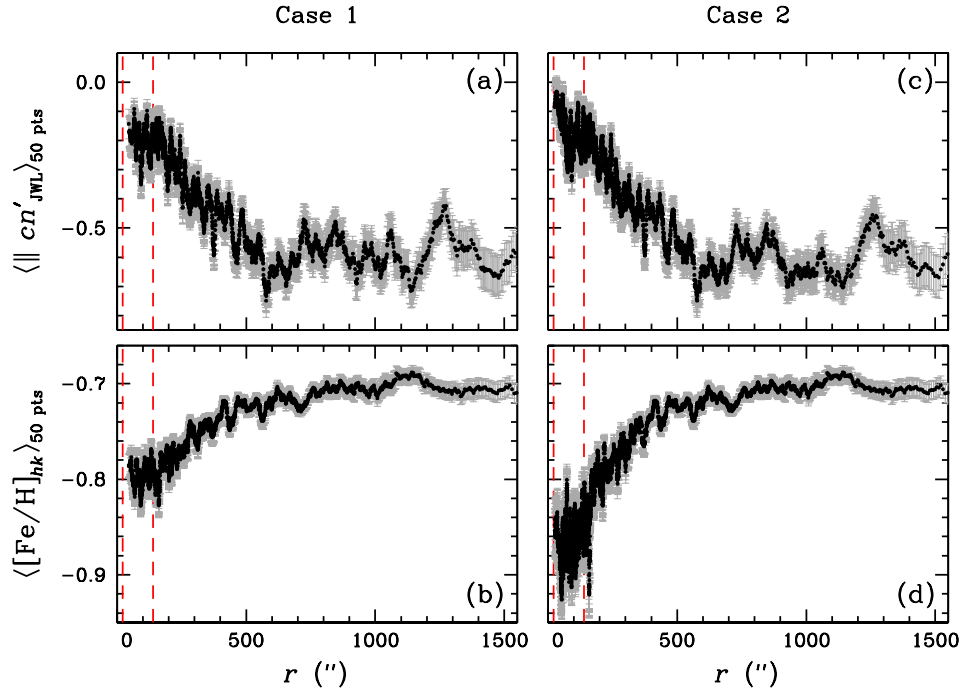


**Figure 14.** (a) The moving average of the adjacent 50 points for the  $\|cn'_{JWL}\|$  index of the proper-motion member RGB stars plotted as functions of radial distance. The vertical thin gray error bars denote the standard error of the mean, and the vertical red dashed lines denote the core and the half-light radii of 47 Tuc. (b) Same as the top panel, but for  $[Fe/H]$ . (c) Same as (a) but for using all RGB stars. (d) Same as (b) but for using all RGB stars.

**Table 8.** Mean and peak RHB  $V$  and  $(b-y)$  from Our Observations and HB Model Simulations.

	CN-w	CN-s	CN-SMP	CN-SMR
Mean $V^1$	$14.052 \pm 0.052 \pm 0.003$	$14.017 \pm 0.050 \pm 0.002$	$14.019 \pm 0.049 \pm 0.002$	$14.002 \pm 0.042 \pm 0.005$
Peak $V^1$	$14.085 \pm 0.010$	$14.039 \pm 0.010$	$14.042 \pm 0.010$	$14.021 \pm 0.010$
Peak $V^2$	$14.077 \pm 0.010$	$14.026 \pm 0.010$	$14.027 \pm 0.010$	$14.015 \pm 0.010$
Peak $V^3$			$13.991 \pm 0.010$	
Peak $V^4$			$13.965 \pm 0.010$	
Mean $(b-y)^1$	$0.538 \pm 0.015 \pm 0.001$	$0.523 \pm 0.018 \pm 0.001$	$0.526 \pm 0.015 \pm 0.001$	$0.493 \pm 0.014 \pm 0.001$
Peak $(b-y)^1$	$0.538 \pm 0.010$	$0.529 \pm 0.010$	$0.529 \pm 0.010$	$0.500 \pm 0.010$
Peak $(b-y)^2$	$0.535 \pm 0.010$	$0.520 \pm 0.010$	$0.520 \pm 0.010$	$0.490 \pm 0.010$
Peak $(b-y)^3$			$0.494 \pm 0.010$	
Peak $(b-y)^4$			$0.500 \pm 0.010$	

<sup>1</sup> From our observations.<sup>2</sup> From synthetic HB model simulations shown in Figure 17.<sup>3</sup> From synthetic HB model simulation using the model isochrone for  $([\text{Fe}/\text{H}], Y, \text{age}) = (-0.8, 0.275, 12.0 \text{ Gyr})$ : case (2) in § 6.3.<sup>4</sup> From synthetic HB model simulation using the model isochrone for  $([\text{Fe}/\text{H}], Y, \text{age}) = (-0.7, 0.300, 12.0 \text{ Gyr})$ : case (3) in § 6.3.

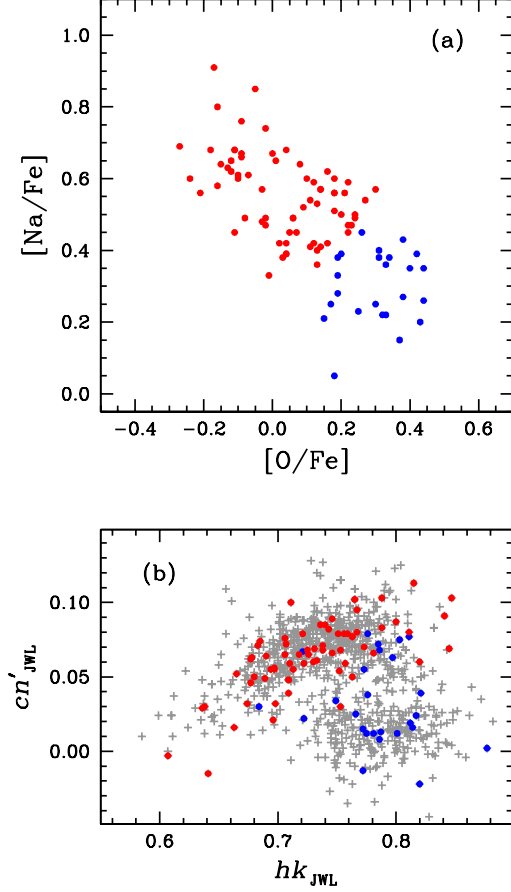


**Figure 15.** (a) A plot of  $[O/Fe]$  versus  $[Na/Fe]$  of the RHB stars in 47 Tuc (Gratton et al. 2013). The blue and red dots denote RHB stars with  $[Na/O] \leq 0.2$  (i.e., equivalent to the CN-w), and  $> 0.2$  dex (i.e., the CN-s), respectively. (b) A plot of  $(b-y)$  versus  $cn'_{JWL}$  of the RHB stars in 47 Tuc along with RHB stars with  $[O/Fe]$  and  $[Na/Fe]$  measurements.

$(\pm 2)\%$  of the total RHB stars, which is roughly consistent with that of the CN-SMP RGB stars,  $\sim 10 (\pm 2)\%$ , within uncertainties. On the other hand, the fraction of the CN-WMP RGB population takes about 3% of the total RGB stars, whose RHB counterpart we do not identify as a separate population in our analysis. The distribution of individual RHB populations in our  $(b-y)$  CMD is consistent with the result of Gratton et al. (2013) that the sodium abundance increases as the  $(B-V)$  color decreases, due to the correlation between the CN and sodium abundances in the cluster (e.g., Cottrell & Da Costa 1981).

In Figure 17(a), we also show isochrones for  $([Fe/H], Y, \text{age}) = (-0.8, 0.275, 12.0 \text{ Gyr})$  and  $(-0.7, 0.300, 12.0 \text{ Gyr})$  to test our ideas for the cases (2) and (3) discussed in §6.3. As shown, these two RHB isochrones fail to explain the CN-SMP(RHB) distribution with satisfaction, and one can rule out these two assumptions. In Figures 17(b)–(c), we show isochrones for  $([Fe/H], Y, \text{age}) = (-0.7, 0.275, 12.0 \text{ Gyr})$  and

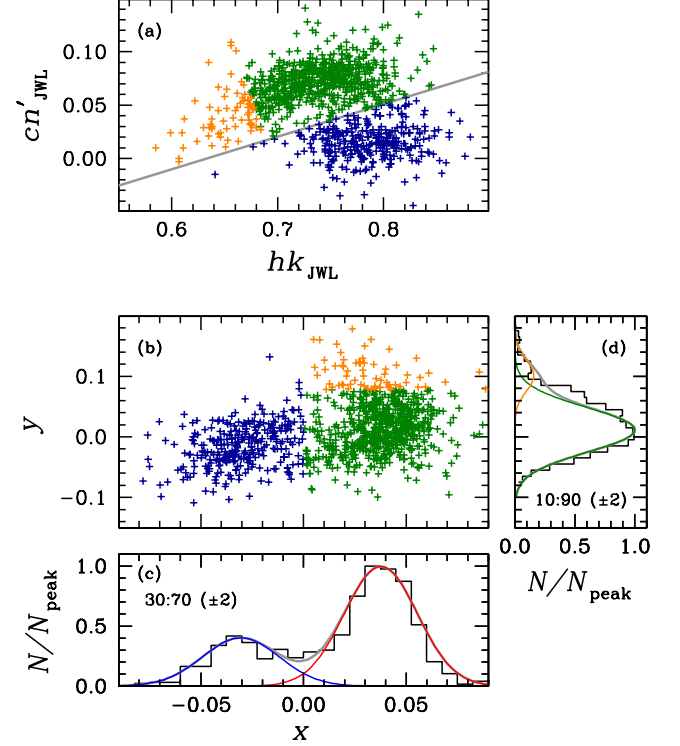


**Figure 16.** (a) A plot of  $hk_{JWL}$  versus  $cn'_{JWL}$  of the RHB stars in 47 Tuc, showing clustered distributions of the RHB stars. The gray solid line denotes the boundary between the CN-w(RHB) and CN-s(RHB) populations. The navy, dark-green, and orange plus signs are for the CN-w(RHB), CN-SMR(RHB), and CN-SMP(RHB), respectively. (b) The RHB distribution on the rotated plane, where the boundary between the two main bodies of the RHB stars in panel (a) is parallel to the vertical axis. (c) The histogram of the RHB stars along the  $x$ -axis, showing a distinctive bimodal distribution. We also show the results returned from our EM estimator. (d) The histogram of the CN-s(RHB) along the  $y$ -axis, showing an asymmetric distribution. We show the results from our EM estimator

$(-0.7, 0.257, 12.0 \text{ Gyr})$ , and they appear to explain the CN-SMR and CN-w RHB populations well.

We calculate the mean and peak  $V$  magnitudes of individual RHB populations, and we show our results in Table 8. Note that the peak magnitudes are determined from the greatest values in their smoothed distribution function with a Gaussian density estimation. The mean color and magnitude of individual populations can be affected by the highly evolved RHB stars. It is believed that the peak color and magnitude determined by their distributions could be more practical to be compared with the model predictions as we will show below. The CN-s(RHB) stars are about 0.3 – 0.4 mag brighter than the CN-w(RHB) stars as we already showed in Figure 17. Our results are in excellent agreement with those by Norris & Freeman (1982), and Briley (1997),  $\sim 0.04 - 0.05 \text{ mag}$ .

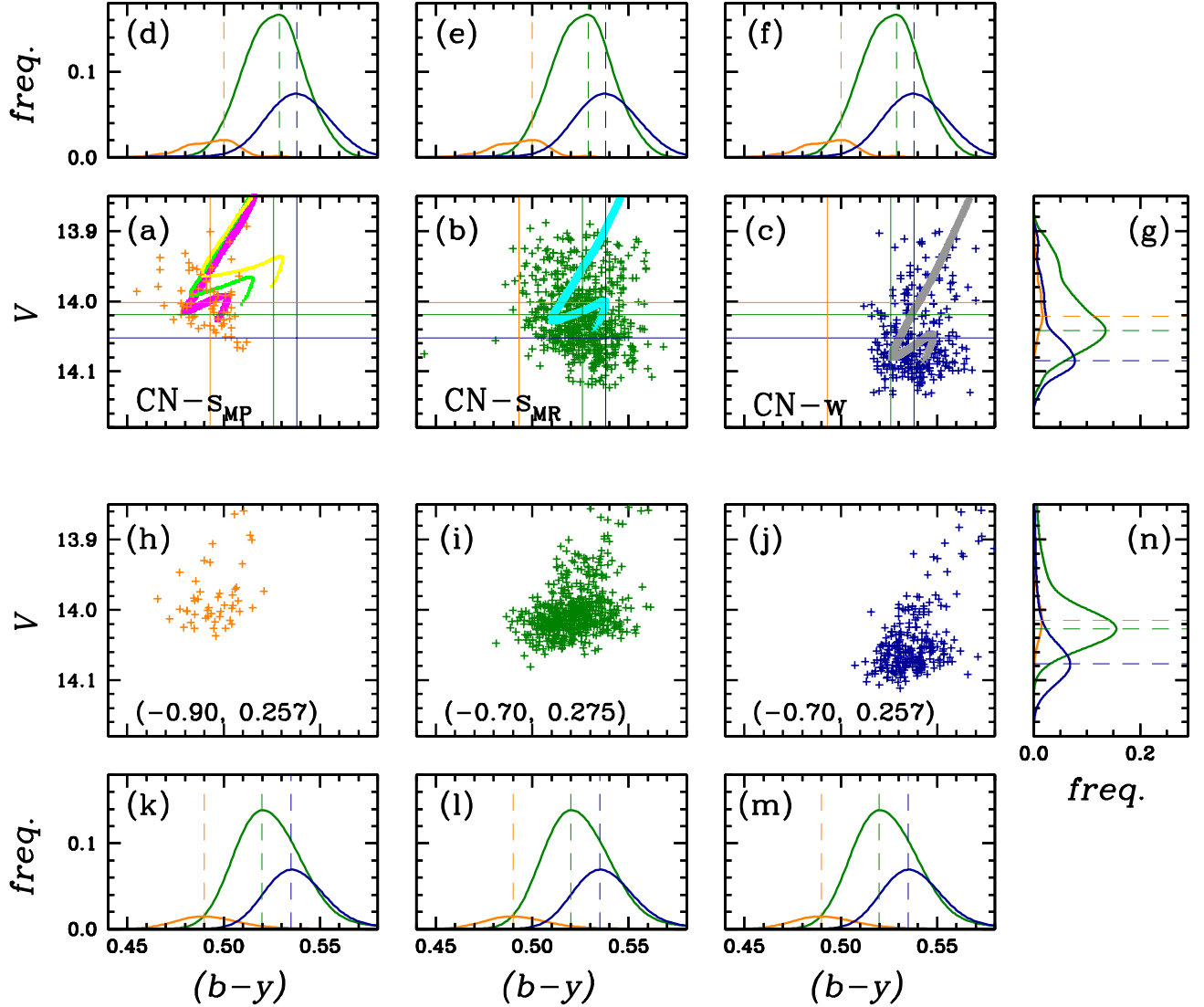


**Figure 17.** (a) A  $(b-y)$  versus  $V$  CMD of the CN-SMP RHB stars in 47 Tuc. The vertical and horizontal thin lines are for the mean  $(b-y)$  and  $V$  of each population: orange (CN-SMP), dark-green (CN-SMR), and navy (CN-w). The thick magenta solid line represents the BaSTI HB isochrone for  $([\text{Fe}/\text{H}], Y, \text{age}) = (-0.9, 0.257, 12.0 \text{ Gyr})$ , while the green and yellow solid lines are for  $(-0.8, 0.275, 12.0 \text{ Gyr})$  and  $(-0.7, 0.300, 12.0 \text{ Gyr})$ . We used the distance modulus of  $(m-M)_0 = 13.21 \text{ mag}$  and the interstellar reddening of  $E(B-V) = 0.03 \text{ mag}$  (Brogaard et al. 2017). (b) Same as (a) but for the CN-SMR RHB stars. The thick cyan solid line represents the BaSTI HB isochrone for  $(-0.7, 0.275, 12.0 \text{ Gyr})$ . (c) Same as (c) but for the CN-w RHB stars. The thick gray solid line represents the BaSTI HB isochrone for  $(-0.7, 0.257, 12.0 \text{ Gyr})$ . (d)–(f) The  $(b-y)$  distributions of each population: orange (CN-SMP), dark-green (CN-SMR), and navy (CN-w). The dashed vertical lines denote the peak  $(b-y)$  values. (g) The  $V$  distributions of each population. The dashed horizontal lines denote the peak  $V$  magnitudes. (h) Synthetic HB models for the CN-SMP RHB stars using the BaSTI model isochrone for  $([\text{Fe}/\text{H}], Y, \text{age}) = (-0.9, 0.257, 12.0 \text{ Gyr})$ . (i) Same as (h) but for CN-SMR RHB stars using the BaSTI model isochrone for  $(-0.7, 0.275, 12.0 \text{ Gyr})$ . (j) Same as (h) but for CN-w RHB stars using the BaSTI model isochrone for  $(-0.7, 0.257, 12.0 \text{ Gyr})$ . (k)–(m) Same as (d)–(f) but for the mean distributions of 1000 synthetic model simulation runs. (n) Same as (g) but for the mean distributions of 1000 synthetic model simulation runs.



The mean  $(b-y)$  color of the CN-s(RHB) stars is  $\sim 0.01 - 0.02$  mag bluer than that of the CN-w(RHB) stars, consistent with the idea that the bulk of the CN-s RHB stars are more helium-enhanced than the CN-w RHB stars are. Since the helium-enhanced RHB population will have smaller total mass and smaller ratio of the envelope mass to the total mass, they will be bluer than those with normal helium abundances (e.g., see [Cassisi & Salaris 2021](#)). We also note that the range of the  $(b-y)$  distribution of the CN-s(RHB) stars is larger than that of the CN-w(RHB) stars, indicating that the CN-s(RHB) stars experience a larger mass-loss dispersion during their RGB evolution, which seems to be odd. It could be also possible that the CN-s(RHB) population contains multiple subpopulations, as we discussed for the RGB stars, the CN-SMP and CN-SMR.

To explore our idea of the existence of the metal-poor RHB component, we constructed the synthetic evolutionary population models using the  $([\text{Fe}/\text{H}], Y, \text{age}) = (-0.7, 0.257, 12.0 \text{ Gyr})$ ,  $(-0.7, 0.275, 12.0 \text{ Gyr})$ , and  $(-0.9, 0.257, 12.0 \text{ Gyr})$  model isochrones for the CN-w, CN-SMR and CN-SMP populations. We performed 1000 trials to calculate the mean  $(b-y)$  color and  $V$  distributions for individual populations along with the peak  $(b-y)$  colors and  $V$  magnitudes. We show our results in Table 8. Although crude, our synthetic models can reproduce the observed peak  $(b-y)$  colors and  $V$  magnitudes. In the table, we also show the results from the  $(-0.7, 0.300, 12.0 \text{ Gyr})$  and  $(-0.8, 0.275, 12.0 \text{ Gyr})$  models for alternative explanations of the CN-SMP population. Our simulations with such models predict brighter peak  $V$  magnitudes and slightly bluer  $(b-y)$  colors than our observations. In Figure 17(h-j), we show the synthetic  $(b-y)$  versus  $V$  CMDs of individual population using one specific trial. We note that the distributions of synthetic models appear to be good for the CN-w and CN-SMP populations. However, the wedge shape of the observed CN-SMR population in the faint magnitude regime cannot be reproduced with a simple stellar population that we used in our study. In the future, more sophisticated HB model simulation would be very desirable (e.g., see [Salaris et al. 2016](#)).

### 7.2. Cumulative Radial Distributions

In Figure 18, we show the CRDs of individual RHB populations. As can be seen in the RGB, the CN-s RHB population is more centrally concentrated than the CN-w RHB, which is not a surprise since the CN-w and CN-s RHB stars are progenies of the CN-w and CN-s RGB stars, respectively. We note that the more centrally concentrated nature of the CN-s RHB stars was also found by [Milone et al. \(2012\)](#).

To quantitatively examine similarity of individual CRDs, we performed the K-S tests, and we show our results in Table 9. When the RGB stars with the whole magnitude range of our interest,  $-1.5 \leq V - V_{\text{HB}} \leq 2.5$  mag, were used, the  $p$ -values related to the CN-w(RHB) population are significantly small, and it can be interpreted that none of the CRDs of the RGB populations were drawn from the same distribution of the CN-w(RHB) population. On the other hand, the CN-s,

CN-SMR and CN-SMP RHB populations show large  $p$ -values with the CN-wMP.

It is thought that the biased sampling in our work may be responsible for this discrepancy. RGB stars were selected from 2.5 mag fainter than the RHB stars are. At the central part of the cluster, where the CN-s population dominates, the degree of incomplete detection of the faint stars would be great and must have affected our individual CRDs. When we restricted the bright RGB stars with  $V \geq 15.0$  mag, the agreement in individual CRDs between the RHB and RGB populations becomes improved, suggesting that each RHB population is the progeny of the corresponding RGB population.

## 8. SUMMARY

In this paper, we presented new large FOV ( $\sim 1^\circ \times 1^\circ$ ) Ca-CN photometry of 47 Tuc (NGC 104). We found that the CN-s population is the major component of the cluster and it is more centrally concentrated than the CN-w population, similar to other Galactic GCs. We obtained the populational number ratios of the RGB and RHB:  $n(\text{CN-w}):n(\text{CN-s}) = 30:70 (\pm 1-2)$ . Our results are in good agreement with those of previous results by others (e.g. [Nataf et al. 2011](#); [Milone et al. 2012](#)).

Following the similar method that we developed in our previous studies ([Lee 2021](#); [Lee & Sneden 2021](#)), we derived the photometric metallicity of individual RGB stars from our  $hk_{\text{JWL}}$  index, finding that both the CN-w and CN-s populations show asymmetric metallicity distributions toward metal-poor regime, and they are well described by bimodal metallicity distributions. In both the CN-w and CN-s populations, the metal-poor components are  $\Delta[\text{Fe}/\text{H}] \sim 0.20$  dex more metal-poor than the metal-rich components, where the metal-rich populations are main components of the clusters. The metal-poor components constitute  $\sim 3\%$  (CN-wMP) and  $\sim 10\%$  (CN-SMP) of the total RGB population. The metal-poor components (i.e., CN-wMP and CN-SMP) are significantly more centrally concentrated than the metal-rich components (i.e., CN-wMR and CN-SMR). In addition, the CN-SMP is more centrally concentrated than the CN-wMP. Therefore, the metal-poor populations themselves mimic the general trend of normal GCs that the CN-s population is the more centrally concentrated than the CN-w.

We investigated the RGBB  $V$  magnitudes, finding that  $V = 14.399 (\pm 0.040)$ ,  $14.559 (\pm 0.025)$ ,  $14.385 (\pm 0.035)$ ,  $14.492 (\pm 0.020)$  mag for the CN-wMP, CN-wMR, CN-SMP, and CN-SMR, respectively, which are in excellent agreement with those analyzed using the photometric data of [Stetson et al. \(2019\)](#). We performed Monte Carlo simulations by means of the evolutionary population synthesis models, showing that the observed RGBB  $V$  magnitudes are consistent with the metallicity difference of  $\Delta[\text{Fe}/\text{H}] \sim 0.15 - 0.20$  dex between the metal-poor and metal-rich components and the helium abundance difference of  $\Delta Y \sim 0.02 - 0.03$  between the CN-wMR and CN-SMR.

Using our photometric indices, we decomposed three RHB populations in 47 Tuc. They are thought to be progenies

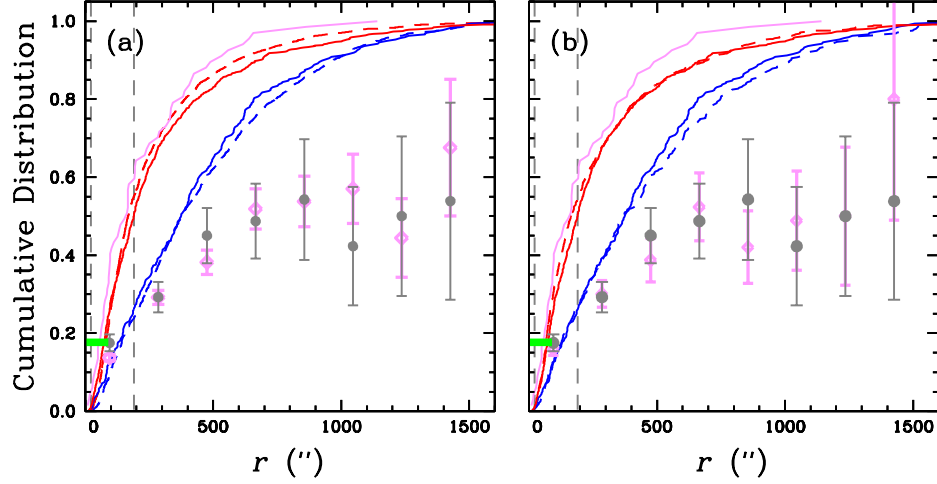


**Figure 18.** (a) CRDs of individual RHB populations (solid lines) along with the whole RGB populations (dashed lines). The blue, red and pink solid lines are for the CN-w(RHB), CN-SMR(RHB) and CN-SMP(RHB) while the blue and red dashed lines are for the CN-w(RGB) and CN-s(RGB). The gray error bars show the fractions of the CN-w RHB population with a binning radial distance of the half-light radius, while the pink error bars show those of the CN-w RGB population. The vertical gray dashed lines denote the core and half-light radii of 47 Tuc. The green-shaded box indicates the fraction of the first generation by Milone et al. (2017) measured in the central part of the cluster. (b) Same as (a) but for the bright RGB stars with  $V \leq 15.0$  mag.

**Table 9.**  $p$  Values Returned from the K-S Tests for the CRDs of individual RHB and RGB populations

	CN-w	CN-WMP	CN-WMR	CN-s	CN-SMP	CN-SMR
All						
CN-w(RHB)	0.026	$3.07 \times 10^{-9}$	0.001	$< 1.00 \times 10^{-15}$	$< 1.00 \times 10^{-15}$	$9.03 \times 10^{-9}$
CN-s(RHB)	$< 1.00 \times 10^{-15}$	0.425	$< 1.00 \times 10^{-15}$	$2.34 \times 10^{-4}$	$< 1.00 \times 10^{-15}$	$< 1.46 \times 10^{-9}$
CN-SMP(RHB)	$1.94 \times 10^{-11}$	0.457	$3.95 \times 10^{-13}$	0.007	$4.76 \times 10^{-4}$	$5.91 \times 10^{-4}$
CN-SMR(RHB)	$< 1.00 \times 10^{-15}$	0.383	$< 1.00 \times 10^{-15}$	0.003	$< 1.00 \times 10^{-15}$	$1.04 \times 10^{-7}$
Bright RGB ( $V \leq 15.0$ mag)						
CN-w(RHB)	0.455	$1.73 \times 10^{-3}$	0.253	$< 1.00 \times 10^{-15}$	$< 1.00 \times 10^{-15}$	$1.77 \times 10^{-12}$
CN-s(RHB)	$< 1.00 \times 10^{-15}$	0.142	$< 1.00 \times 10^{-15}$	0.074	$< 1.00 \times 10^{-15}$	0.219
CN-SMP(RHB)	$9.52 \times 10^{-8}$	0.719	$2.31 \times 10^{-8}$	0.668	$1.47 \times 10^{-7}$	0.129
CN-SMR(RHB)	$< 1.00 \times 10^{-15}$	0.118	$< 1.00 \times 10^{-15}$	0.041	$< 1.00 \times 10^{-15}$	0.319

of the CN-WMR, CN-SMP, and CN-SMR based on the CN strengths and comparisons with the RHB model isochrones. Good agreements in the CRDs of RHB stars with those of the bright RGB stars may support our conclusion. It is believed that, due to its very small fraction, the RHB counterpart of the CN-WMP cannot be clearly seen.

Recently, McKenzie & Bekki (2021) conducted numerical simulations for the formation of a 47 Tuc-like GC in a dwarf galaxy environment. Their result indicated that newly formed GCs should be able to retain some low-mass field stars from their parent galaxy. The metal-poor components (i.e., CN-WMP and CN-SMP) that we found in this work could be field

stars surrounding the CN-WMR and CN-SMR. However, the carbon and nitrogen abundance difference between the CN-WMP and CN-SMP cannot be easily explained in the context of the chemical evolution of the disk stars in dwarf galaxies, where the C–N anticorrelation does not appear to exist. Instead, the metal-poor components could be understood by an independent GC system that merged with the more massive metal-rich component as we suggested for M22 and M3 (e.g., Lee 2015, 2020; Lee & Sneden 2021). The fraction of the metal-poor stars in our study is about 13%, which can be translated into the total mass of  $\sim 1.0 \times 10^4 M_{\odot}$  (Baumgardt & Hilker 2018). In such a small mass system, it

would be natural to expect no helium enhancement between the CN- $w_{MP}$  and CN- $s_{MP}$  populations (e.g., see [Milone et al. 2018b](#)), which is exactly what we observed in 47 Tuc.

#### ACKNOWLEDGMENTS

J.-W.L. thanks Professor Y.-C. Kim at Yonsei University for the discussion on the  $Y^2$  isochrones and Drs. A.A.R. Valcarce and M. Catelan at Pontificia Universidad Católica de Chile for reviving the PGPUC online service after the tragic fire accident that heavily affected the Institute for Astrophysics. He also thanks an anonymous referee for a careful review of the manuscript and many priceless suggestions. J.-W.L. acknowledges financial support from the Basic Science Research Program (grant No. 2019R1A2C2086290) through the National Research Foundation of Korea (NRF) and from the faculty research fund of Sejong University in 2019.

#### REFERENCES

- Anthony-Twarog, B. J., Laird, J. N., Payne, D., & Twarog, B. A. 1991, *AJ*, 101, 1902
- Anderson, J., Piotto, G., King, I. R., Bedin, L. R., Guhathakurta, P. 2009, *ApJL*, 697, L58
- Bastian, N., Cabrera-Ziri, I., & Salaris, M. 2015, *MNRAS*, 449, 3333
- Bastian, N., & Lardo, C. 2018, *ARA&A*, 56, 3
- Bekki, K. 2019, *A&A*, 622, 53
- Bragaglia, A., Carretta, E., Gratton, R., et al. 2010 *A&A*, 519, 60
- Baumgardt, H., & Hilker, M. 2018, *MNRAS*, 478, 1520
- Briley, M. M. 1997, *AJ*, 114, 1051
- Briley, M. M., Harbeck, D., Smith, G. H., Grebel, E. K. 2004, *AJ*, 127, 1588
- Briley, M. M., Hesser, J. E., & Bell, R. A. 1991, *ApJ*, 373, 482
- Brogaard, K., VandenBerg, D. A., Bedin, L. R., et al. 2017, *MNRAS*, 468, 645
- Calura, F., D’Ercole, A., Vesperini, E., Vanzella, E., & Sollima, A. 2019, *MNRAS*, 489, 3269
- Cannon, R. D., Croke, B. F. W., Bell, R. A. et al. 1998, *MNRAS*, 298, 601
- Carney, B. W. 1996, *PASP*, 108, 900
- Carretta E., Bragaglia, A., Gratton, R.G., et al. 2009, *A&A*, 505, 117
- Carretta E., Gratton, R.G., Bragaglia, A., et al. 2004, *A&A*, 416, 925
- Cassisi, S., & Salaris, M. 1997, *MNRAS*, 285, 593
- Cassisi, S., & Salaris, M. 2013, *Old Stellar Populations: how to study the fossil record of galaxy formation* (Berlin:Wiley-VCH)
- Cassisi, S., & Salaris, M. 2020, *A&AS*, 28, 5
- Cassisi, S., & Salaris, M., Pietriferni, A. et al. 2008, *ApJL*, 672, L115
- Chun, M. S., & Freeman, K. C. 1979, *ApJ*, 227, 93
- Cottrell, P. L., & Da Costa, G. S. 1981, *ApJL*, 245, L79
- Codero, M. J., Pilachowski, C. A., Johnson, C. I., et al. 2014, *ApJ*, 780, 94
- D’Ercole, A., Vesperini, E., D’Antona, F., McMillan, S. L. W., & Recchi, S. 2008, *MNRAS*, 391, 825
- Di Criscienzo, M., Vettura, P., D’Antona, F. et al. 2010, *MNRAS*, 408, 999
- Dondoglio, E., Milone, A. P., Lagioia, E. P. et al. 2121, *ApJ*, 906, 21
- Dotter, A., Chaboyer, B., Jevremović, D., Kostov, V., Baron, E., Ferguson, J. W. 2008, *ApJS*, 178, 89
- Fare, A., Webb, J. J., & Sills, A. 2018, *MNRAS*, 481, 3027
- Gaia Collaboration, Brown, A. G. A., Vallenari, A., et al. 2021, *A&A*, 649, A1
- Girardi, L., Bertelli, G., Bressan, A. et al. 2002, *A&A*, 391, 195
- Gratton, G. R., Bragaglia, A., Carretta, E. et al. 2019, *A&AS*, 27, 8
- Gratton, G. R., Lucatello, S., Sollima A., et al. 2013, *A&A*, 549, A41
- Harbeck, D., Smith, G. H., Grebel, E. K. 2003, *AJ*, 125, 197
- Hesser, J. E., Harris, W. E., Vandenberg, D. A., et al. 1987, *PASP*, 99, 739
- Hesser, J. E. 1978, *ApJL*, 223, L117
- Kurucz, R. L. 2011, *Can. J. Phys.*, 89, 417
- Lacchin, E., Calura, F., & Vesperini, E. 2021, *MNRAS*, 506, 5951
- Lagioia, E. P., Milone, A. P., Marino, A. F., et al. 2018, *MNRAS*, 475, 4088
- Lardo, C., Salaris, M., Cassisi, S., & Bastian, N. 2022, *A&A*, 662, 117
- Lee, J.-W. 2010, *MNRAS*, 405, L36
- Lee, J.-W. 2015, *ApJS*, 219, 7

- Lee, J.-W. 2016, *ApJS*, 226, 16
- Lee, J.-W. 2017, *ApJ*, 844, 77
- Lee, J.-W. 2018, *ApJS*, 238, 24
- Lee, J.-W. 2019a, *ApJ*, 872, 41
- Lee, J.-W. 2019b, *ApJL*, 875, L27
- Lee, J.-W. 2019c, *ApJ*, 883, 166
- Lee, J.-W. 2020, *ApJL*, 888, L6
- Lee, J.-W. 2021, *ApJL*, 918, L24
- Lee, J.-W., & Carney, B. W. 1999, *AJ*, 117, 2868
- Lee, J.-W., Kang, Y.-W., Lee, J., & Lee, Y.-W. 2009, *Nature*, 462, 480
- Lee, J.-W., López-Morales, M., Hong, K. et al. 2014, *ApJS*, 210, 6
- Lee, J.-W., & Pogge, R. 2016, *JKAS*, 49, 289
- Lee, J.-W., & Sneden, C. 2021, *ApJ*, 909, 167
- Legnardi, M. V., Milone, A. P., Armillotta, L., et al. 2022, *MNRAS*, 513, 735
- Marino, A. F., Milone, A. P., Casagrande, L., et al. 2016, *MNRAS*, 459, 610
- Marino, A. F., Milone, A. P., Renzini, A., et al. 2019, *MNRAS*, 487, 3815
- McKenzie, M., & Bekki, K. 2021, *MNRAS*, 500, 4578
- Milone A. P., Bedin, L.R., Piotto, G. et al. 2008, *ApJ*, 673, 241
- Milone A. P., Marino, A. F., Mastrobuno-Battisti, A., & Laagioia, E. P. 2018a, *MNRAS*, 479, 5005
- Milone A. P., Marino, A. F., Renzini, A. et al. 2018b, *MNRAS*, 481, 5098
- Milone A. P., Piotto, G., Bedin, L.R. et al. 2012, *ApJ*, 744, 58
- Milone A. P., Piotto, G., Renzini, A. et al. 2017, *MNRAS*, 464, 3636
- Nataf, D. M., Gould, A., Pinsonneault, M. H., & Stetson, P. B. 2011, *ApJ*, 736, 94
- Norris, J., & Freeman, K. C. 1979, *ApJL*, 230, L179
- Norris, J., & Freeman, K. C. 1982, *ApJ*, 254, 143
- Pietrinferni, A., Hidalgo, S., Cassisi, S., Salaris, M., et al. 2021, *ApJ*, 908, 102
- Renzini, A., D’Antona, F., Cassisi, S. et al. 2015, *MNRAS*, 454, 4197
- Renzini, A., & Fusi Pecci, F. 1988, *ARA&A*, 26, 199
- Salaris, M., Cassisi, S., & Pietrinferni, A. 2016, *A&A*, 590, 64
- Sbordone, L., Salaris, M., Weiss, A., & Cassisi, S. 2011, *A&A*, 534, A9
- Smith, H. A. 1979, *AJ*, 84, 176
- Stetson P. B. 1987, *PASP*, 99, 191
- Stetson P. B. 1994, *PASP*, 106, 250
- Stetson P. B., Pancino, E., Zocchi, A. et al. 2019, *MNRAS*, 485, 3042
- Vesperini, E., Hong, J., Giersz, M., & Hypki, A. 2021, *MNRAS*, 502, 4290
- Wang, Y., Primas, F., Charbonnel, C. et al. 2017, *A&A*, 607, 135
- Yi, S., Kim, Y.-C., Demarque, P., et al. 2008, in *Proc. IAU Symp.* 252, *The Art of Modeling Stars in the 21st Century*, ed. L. Deng & K. L. Chan (Cambridge: Cambridge Univ. Press), 413